Title
Geostatistical analysis of the effects of stage and roughness on reach-scale spatial patterns of velocity and turbulence intensity

Journal
Geomorphology, 83

Authors
Legleiter, Carl J.
Phelps, Tracy L.
Wohl, Ellen E.

Publication Date
2007

DOI
10.1016/j.geomorph.2006.02.022

Peer reviewed

Geostatistical analysis of the effects of stage and roughness on reach-scale spatial patterns of velocity and turbulence intensity

Carl J. Legleiter*, Tracy L. Phelps,† and Ellen E. Wohl
Department of Geosciences, Colorado State University, Fort Collins, CO 80523

Submitted to *Geomorphology* 23 April 2005; revised 23 September 2005

Abstract

Although previous research has documented well-organized interactions between the turbulent flow field and an irregular boundary, the spatial variability of turbulent flow characteristics at the reach scale remains poorly understood. In this paper, we present detailed field measurements of three-dimensional flow velocities and turbulence intensities in a high-gradient, cobble-bed riffle from three discharges; additional data on sediment grain size and bed topography were used to characterize boundary roughness. An acoustic Doppler velocimeter was used to measure velocities along five cross-sections within a 6 m long reach of the North Fork Cache La Poudre River; vertical profiles were also measured along the channel thalweg. We adopted a spatially explicit stochastic hydraulic approach and focused not on coherent flow structures *per se* but rather time-averaged, reach-scale variability and spatial pattern. Scaling velocities and turbulence intensities by the reach-averaged friction velocity U_* accounted for changes in flow depth and enabled comparisons among the three discharges. We quantified the effects of stage and roughness by assessing differences among probability distributions of hydraulic quantities and by examining geostatistical metrics of spatial variability. We computed semivariograms for both the streamwise and transverse directions and fit parametric models to summarize the spatial structure of each variable at each discharge. Cross-correlograms were also used to describe the local and lagged effects of boundary roughness on flow characteristics. Although the probability distributions yielded some insight, incorporating spatial information revealed important elements of stage-dependent flow structure. The development of secondary currents and flow convergence at higher stages was clearly documented in maps and semivariograms. In general, the spatial structure of the flow field became smoother and more continuous as stage increased and the effects of boundary roughness diminished. Although roughness elements do influence velocities and turbulence intensities, our data suggest that the flow primarily responds to the gross morphology of the channel and that flow depth is the primary control on flow structure. The geostatistical framework proved useful, and our results indicate that a complete stochastic description must also be explicitly spatial.

* *Corresponding author, current address*: C.J. Legleiter, Geography Department, University of California Santa Barbara, Ellison Hall 3611, Santa Barbara, CA 93106; E-mail: carl@geog.ucsb.edu
† *Current address*: Herrera Environmental Consultants, 2200 Sixth Avenue 1100, Seattle, WA 98121

1 Introduction

Interactions between a turbulent flow field and an irregular, mobile boundary control the erosion, transport, and deposition of sediment. These interactions occur across a range of spatial scales and ultimately define the morphology of alluvial channels and the physical habitat template for aquatic biota (Clifford and French, 1993a; Nikora and Smart, 1997; Booker et al., 2001). Several decades of research in flume and field environments have resulted in useful theoretical and empirical relations between bed material properties, flow resistance, and hydraulic quantities, but most of these studies have considered sand- or gravel-bed channels with low to moderate gradients. The extent to which these results apply to steeper, coarser-grained natural rivers remains unclear due to a paucity of basic field data from such environments and, we suggest, the lack of appropriate, spatially explicit analytical frameworks.

In coarse-grained channels, sediment particles occupying a significant proportion of the flow depth represent an important source of flow resistance that affects the shape of vertical velocity profiles (Wiberg and Smith, 1991; Byrd et al., 2000; Lawless and Robert, 2001a). Velocity and turbulence in these streams is typically dominated by flow separation and eddy shedding in the lee of obstacles as momentum is exchanged between low-velocity, near-bed fluid and faster flow outside the roughness layer (Best, 1993; Buffin-Belanger and Roy, 1998). Over the past decade, significant effort has been directed toward the periodic, organized spatiotemporal patterns of macroturbulence known as coherent flow structures. Roy et al. (2004) reviewed this body of literature and presented detailed field measurements suggesting that these structures occupy the entire flow depth, with streamwise lengths and transverse widths of 3 to 5 and 0.5 to 1 times the flow depth, respectively. Their data also indicated strong interaction between the outer flow and the near-bed region, consistent with an emerging model of oblique high- and low-speed wedges associated with sweeps of high-momentum fluid toward the bed and ejections of low-momentum fluid upward toward the free surface (Ferguson et al., 1996; Roy, Buffin-Belanger and Deland, 1996; Buffin-Belanger et al., 2000). These macroturbulent structures play an important role in sediment transport (e.g., Shvidchenko and Pender, 2001; Wu and Yang, 2004) and persist in the presence of roughness transitions (Robert et al., 1996), protruding clasts (Kirkbride, 1993; Smart, 1994; Buffin-Belanger and Roy, 1998; Lawless and Robert, 2001b), and various bedforms as the flow responds to different scales of topographic variability (Clifford et al., 1992; Clifford, 1996; Lawless and Robert, 2001a).

While these studies have improved our understanding of the fine-scale, high-frequency fluid mechanical processes operating within turbulent boundary layers, they have also been limited in several important respects. Widely used electromagnetic current meters provide only two components of velocity, most often the streamwise and vertical, and field data sets typically consist of only a few profile measurements along downstream transects (e.g., Robert et al., 1996). While some researchers have addressed the lateral dimension (e.g., Lawless and Robert, 2001b; Roy et al., 2004), their measurements have not spanned the entire width of natural channels. In general, the difficulty of acquiring detailed measurements of flow velocity and bed elevation under field conditions has limited the spatial extent of previous studies, and our knowledge of the variability and spatial pattern of velocity and turbulence intensity at the reach scale remains incomplete. In a recent study similar to ours, Lamarre and Roy (2005) collected the most spatially extensive field data set of which we are aware and concluded that roughness elements had surprisingly little impact on the flow at the reach scale — velocity profiles were predominantly log-linear and protuberant clasts had only localized effects on the flow. The results of Lamarre and Roy (2005) suggested that, despite a topographically complex channel boundary featuring large roughness elements, the spatial variability of turbulent flow characteristics at the reach scale remained organized – the flow field was dominated by coherent patterns associated with large-scale variations in depth rather than by abrupt, isolated changes associated with individual clasts.

To quantify such reach-scale patterns, we adopted the stochastic hydraulic approach pioneered by Lamouroux and colleagues (1995; 1998) and subsequently used for in-stream habitat assessment by Rhoads et al. (2003). Under this framework, point measurements of appropriately scaled hydraulic quantities are described in terms of probability distributions, the parameters of which vary as functions of discharge (Lamouroux, 1998) or reach-scale geomorphic descriptors (Lamouroux et al., 1995). Stewardson and McMahon (2002) extended the work of Lamouroux by developing a stochastic model for the joint variation of depth and velocity and found that the shape of this distribution was strongly dependent on channel morphology. This result suggests that a complete stochastic description must also be spatially explicit. An existing, theoretically grounded discipline – geostatistics – is ideally suited to this task, and its application to the study of channel change has recently been demonstrated (Chappell et al., 2003). Chappell et al. (2003) used a geostatistical measure of spatial variability called the semivariogram (e.g., Robert and Richards, 1988) to summarize and interpret the morphodynamics of a gravel-bed river over different time periods. In this study, we use semivariogram models to quantify changes in the reach-scale spatial structure of flow characteristics with increasing discharge. While previous turbulence research has primarily adopted correlation-based approaches which are independent of the units of measurement (e.g, Robert et al., 1993), the standardization inherent to these calculations obscures the magnitude of variation. To compare the variability of flow characteristics at different discharges we first scale our velocity data by a reach-averaged measure of flow strength and then use the resulting non-dimensional quantities to compute semivariograms that preserve information on the magnitude of variation while also providing an indication of spatial structure.

In this paper, we present detailed, spatially distributed field measurements of flow velocity and turbulence intensity from a cobble-bed riffle at three different discharges. We focus not on coherent flow structures *per se* but rather time-averaged, reach-scale spatial patterns of flow characteristics in a high-gradient, coarse-grained mountain river. Our objectives are twofold: (1) use geostatistical techniques to summarize changes in the spatial variability of velocity and turbulence intensity with increasing discharge; and (2) examine the effects of bed topography and large roughness elements on flow structure at the reach scale. We seek to quantify the extent to which the organized spatial patterns of velocity dictated by the governing equations persist in the presence of irregular topography and coarse bed material using data spanning the full channel width, a distance of several meters in the streamwise direction, and a range of discharges.

2 Methods

2.1 Field data collection

Between June 2001 and April 2003, we measured bed topography, surface particle size, and three-dimensional flow velocity in a cobble-bed riffle on the North Fork Cache La Poudre River in Colorado. Our study reach is located in Phantom Canyon, approximately 55 km northwest of Fort Collins, where the North Fork has incised a 140-m deep canyon into Precambrian granite exposed in the foothills of the Rocky Mountain Front Range (Figure 1). The drainage area is 1470 km^2 and the snowmelt-dominated hydrograph is regulated by Halligan Dam, 2.5 km above our study site. Spring runoff spilling over the dam produces peak flows that averaged 14.67 m^3/s over the period 1999-2004 (USGS gauge 067511150), but base flows less than 1 m^3/s persist for much of the year and suspended and bedload transport rates are minimal. This bedrock-controlled channel features a well-defined sequence of pools, associated with lateral constrictions formed by bedrock outcrops, and riffles consisting of cobble and boulder alluvium. The mean width of the North Fork is 14 m and the average gradient of 0.011 increases to 0.04 in some riffles (Wohl and Legleiter, 2003). We selected a single, straight riffle and collected data at three different discharges (Table 1) along five 17-m wide cross-sections with a streamwise spacing of 1.5 m; cross-sections were numbered sequentially downstream. We measured velocities at stations located every 0.5 m along all five cross-sections at 1.13 and 2.41 m^3/s and sections 1-4 for a high flow data set during which discharge varied between 3.0 - 3.6 m^3/s, producing only minor changes in stage, with a mean of 3.25 m^3/s. These flows correspond to 6.7, 14.4, and 19.5% of the mean annual flood, but the study reach is effectively inaccessible by wading at discharges greater than 4 m^3/s. No flows capable of mobilizing the coarse bed material occurred during our study, and the channel morphology remained stable.

A SonTek FlowTracker acoustic Doppler velocimeter (ADV) was used to measure three–dimensional velocities based on the Doppler frequency shift between emitted acoustic pulses and their reflection from material suspended within a 0.25 cm^3 sampling volume located 10 cm from the instrument (SonTek, 2000). Acoustic doppler technology is an established method of measuring turbulent flow in rivers, and the operating principles have been described elsewhere (Lane et al., 1998; Voulgaris and Trowbridge, 1998; McLelland and Nicholas, 2000). In our study, the ADV was mounted on a top-setting wading rod and oriented perpendicular to each cross-section. This alignment ensured a consistent frame of reference among cross-sections and discharges, and the sensor was parallel to the primary streamwise flow in most cases. We did not apply a rotation to our ADV data, consistent with the suggestion of Roy, Biron and DeSerres (1996) and the protocol of Lamarre and Roy (2005). The FlowTracker measured velocity at a frequency of 10 Hz and (internally) averaged the signal to 1 Hz (SonTek, 2000); 180 s time series were recorded at each station. The low, 1 Hz sampling frequency represented an important instrumental limitation (Soulsby, 1980), and we were unable to infer specific characteristics of turbulence (i.e., higher-order moments, autocorrelation functions, or power spectra). The 180 s record length allowed for averaging over the passage of several flow structures (Babaeyan-Koopaei et al., 2002), however, and, rather than performing detailed, time-domain analyses of individual measurement locations as in previous studies (e.g., Roy et al., 2004), we used the resulting summary statistics to characterize reach-scale spatial patterns of velocity and turbulence intensity. For the cross-sectional deployment, we approximated the depth-averaged velocity by assuming a logarithmic velocity profile and placing the ADV at 0.6 of the flow depth h where $h < 45$ cm and at $0.2h$ and $0.8h$ where $h > 45$ cm (Whiting, 2003); summary statistics computed for the two depths were then averaged to provide a single data point for the plan view location. In a second, longitudinal deployment, we measured vertical profiles where each cross-section intersected the channel thalweg. Each of these profiles consisted of eight measurements equally spaced between $0.1h$ and $0.8h$ above the bed.

ADV measurements are subject to several sources of error, particularly in steep, coarse-grained channels, and must be filtered before calculating flow statistics (Lane et al., 1998; McLelland and Nicholas, 2000; Goring and Nikora, 2002). Along with the 1 Hz velocity data, the FlowTracker recorded a signal-to-noise ratio (SNR) for each of the three acoustic pulses, which we used to discard observations for which the SNR was outside the acceptable range of 10-35 dB specified by the manufacturer (SonTek, 2000). Similarly, we removed spikes which were more than three standard deviations from the mean of the 180 s time series. The remaining data were then visually inspected to remove artifacts related to aliasing, in which the instantaneous velocity exceeds the ADV's dynamic range and results in a very high value followed by a very low value. The points we rejected from the individual time series were replaced by cubic spline interpolation. Although more sophisticated filtering schemes have been developed (Goring and Nikora, 2002), they are intended for data collected at higher sampling frequencies and can be problematic when spikes occur in succession, as was often the case with our data. The number of velocity data removed by this conservative filtering process varied among stations and differed for the three velocity components, with the vertical typically less reliable than the streamwise and transverse velocities. Data quality tended to be poorest for near-bed measurements and where velocities were high (> 100 cm/s), possibly due to acoustic reflections from the substrate (SonTek, 2000), shear within the sampling volume (Finelli et al., 1999), and/or interference from air bubbles (Rodriguez et al., 1999). The difficulty of accurately positioning the sampling volume close to an irregular boundary and the generally low quality of near-bed data also prevented us from including more closely spaced measurements in our vertical profiles and precluded estimation of boundary shear stresses (e.g., Biron et al., 1998). We excluded measurement stations for which more than 10% of the instantaneous velocity data were removed for any one of the three components, and stringent application of this criterion resulted in the rejection of 8 to 19% of the measurement stations for the cross-sectional deployment and 12 to 20% of the thalweg profile points (Table 2).

In addition to the velocity data, we also characterized surface particle size and channel bed topography within the riffle. Intermediate clast diameters were measured *in situ* every 0.25 m along each cross-section and used to derive the reach-averaged grain size distribution given in Table 3. We used a total station laser theodolite to obtain 1060 measurements of bed elevation distributed throughout the reach for a density of 8.31 points/m^2. Points located 0.5, 1.0, and 1.5 m upstream of each velocity station were surveyed to estimate local approach gradients, the mean of which yielded a reach-averaged channel bed slope of 0.041. We used these data to obtain a continuous topographic representation of the channel by kriging with a trend. This geostatistical technique accounts for a trend (i.e., bed slope) described as a function of the coordinates and then uses the spatial covariance structure of the residuals from this trend in assigning weights to the available data so as to provide unbiased, (least-squares) optimal estimates of bed elevation at unsampled locations (Goovaerts, 1997); Chappell et al. (2003) used a similar approach to modeling bed topography. We derived a trend model that was linear in the streamwise direction and quadratic in the transverse direction by ordinary least squares regression and used the residuals from this trend to compute an omni-directional residual semivariogram (Figure 2). The corresponding covariance model was then inserted into the kriging with a trend system of equations to predict elevations on a regular 5 cm by 5 cm grid. All of our analyses were performed using custom functions written in the MATLAB programming language.

2.2 Calculation of hydraulic quantities

Our analysis of velocity and turbulence patterns within the riffle considered six fundamental hydraulic quantities. Following Nezu and Nakagawa (1993), we resolved the instantaneous velocity vector into three orthogonal components which were in turn decomposed as the sum of a time-averaged mean velocity and (zero-mean) fluctuations about this average; our notation is summarized in Table 4. Turbulence intensities for each velocity component were quantified by computing root mean square (RMS) values from the ADV time series data (Clifford and French, 1993b). In order to compare flow fields for the three discharges we sampled, we did not use the mean velocity and turbulence intensity components directly but rather scaled them by the friction velocity $U_* = \sqrt{g\bar{h}S}$ (Nezu and Nakagawa, 1993; Babaeyan-Koopaei et al., 2002), where g is gravitational acceleration, $\bar{h}$ is the reach-averaged depth (mean of depths measured at velocity measurement stations), and S is (approximated by) the reach-averaged channel bed slope of 0.041. Scaling the velocity components by U_* thus accounted for the effects of increasing flow stage on the depth-averaged velocity.

We examined the effects of bed roughness on velocity and turbulence intensity by computing a local roughness index from our topographic data set. We developed an algorithm to identify all survey points within a rectangular region extending 1.25 m upstream, 0.25 m downstream, and 0.3 m to either side of each velocity measurement station and computed the local roughness height k_s as the standard deviation of these bed elevation measurements. Although roughness is typically expressed in terms of some percentile of the sediment grain size distribution, our index of topographic variability provided a more appropriate, site-specific measure of the topographic variability representing various scales of flow resistance [see Nikora et al. (1998) for a discussion of this random field-based approach and Lane (2005) for a discussion of the role of topography in roughness characterization]. The median of 98 k_s values was 67 mm, which compares favorably with the bed surface D_{50} of 124 mm if, on average, approximately half of the intermediate clast diameter protrudes above the mean bed elevation. A stage-dependent, local measure of relative roughness at each velocity measurement location was then computed as h/k_s, analogous to the reach-averaged R/D_{84} used in previous studies, where R is the hydraulic radius.

2.3 Geostatistical analysis

The spatial patterns of velocity and turbulence intensity we measured during our cross-sectional deployment were quantified using a pair of geostatistical metrics. First, the spatial structure of individual flow variables was described in terms of the semivariogram

$$\gamma(\mathbf{h}) = \frac{1}{2N(\mathbf{h})} \sum_{\alpha=1}^{N(\mathbf{h})} [z(\mathbf{s}_\alpha) - z(\mathbf{s}_\alpha + \mathbf{h})]^2, \tag{1}$$

where $\mathbf{h}$ is the lag vector separating pairs of observations of the random variable z at locations given by the coordinate vectors $\mathbf{s}_\alpha$ and $\mathbf{s}_\alpha + \mathbf{h}$, and $N(\mathbf{h})$ is the number of pairs with separation vectors encompassed by a specified range of distances and directions centered about $\mathbf{h}$ (Goovaerts, 1997). Evaluating Equation 1 for various lag vectors $\mathbf{h}$ yields an experimental semivariogram that describes dissimilarity (the average squared difference between observations) as a function of distance. Smaller values of $\gamma(\mathbf{h})$ at a given $\mathbf{h}$ indicate stronger spatial auto-correlation — that is, a lower spatial frequency or smoother 'texture'. Directional semivariograms can be computed by restricting the angular tolerance about $\mathbf{h}$ and specifying a maximum horizontal band width for the search sector; for more detail, see Deutsch and Journel (1998). In this study, we referenced our measurements to Smith and McLean's (1984) channel-centered (s, n) coordinate system and calculated streamwise (s) and transverse (n) directional semivariograms for the six non-dimensional hydraulic quantities listed in Table 4. The lags and tolerances we used are given in Table 5.

Although these semivariograms provided useful univariate spatial descriptions, we sought to more concisely and generally describe the spatial structure of velocity and turbulence by fitting parametric covariance models to these experimental data. The covariance $C(\mathbf{h})$ and semivariogram are linked by the relation $\gamma(\mathbf{h}) = C(0) - C(\mathbf{h})$; the correlogram $\rho(\mathbf{h})$ used in previous fluvial studies (e.g., Robert et al., 1993; Roy et al., 2004) can be obtained by dividing through by $C(0)$, which represents the (stationary) variance of the data. Ensuring a non-negative variance implies that only certain, positive definite covariance models are permissible, and in this study we considered nugget, exponential, and Gaussian models:

$$C_{nug}(\mathbf{h}) = \begin{cases} 0 & \text{when } |\mathbf{h}| = 0 \\ b & \text{when } |\,\mathbf{h}| > 0 \end{cases} \quad (2)$$

$$C_{exp}(\mathbf{h}) = b \exp\left(\frac{-3|\mathbf{h}|}{a}\right) \quad (3)$$

$$C_{Gauss}(\mathbf{h}) = b \exp\left(\frac{-3|\mathbf{h}|^2}{a}\right), \quad (4)$$

where b is the sill and a is a non-linear parameter called the range; individual models can be combined to form nested structures (i.e., nugget + Gaussian; Goovaerts, 1997). Because the exponential and Gaussian models asymptotically approach the sill, a corresponds to the lag distance at which the model value reaches 95 % of the sill (Wackernagel, 2003). These parameters are illustrated in Figure 2 and can be interpreted as follows (Oliver and Webster, 1986; McBratney and Webster, 1986): 1) a nugget effect is a discontinuity at the origin of the semivariogram due to measurement error, fine-scale variability not captured by the sampling strategy, or a lack of spatial correlation; 2) the sill is the ordinate value at which the semivariogram stops increasing and is equal to the overall variance of the data; and 3) the range is the lag distance at which the sill is reached; pairs of observations separated by distances greater than the range are no longer spatially correlated with one another. The exponential model increases more rapidly as $|\mathbf{h}|$ increases than does the Gaussian covariance and thus indicates a less 'smooth' spatial structure for fixed a and b.

In physical terms, the semivariogram describes differences in velocity as a function of distance and is therefore related to the gradient, and to the (stage-dependent) convective terms in the governing equations (Whiting and Dietrich, 1991; Whiting, 1997). The sill and range of a covariance model thus provide information on the magnitude of velocity variations and the characteristic spatial scale over which these variations occur. Similarly, physical interpretations can be assigned to each of the covariance models we considered. A pure nugget effect implies a lack of spatial correlation and might be expected to occur if large roughness elements precluded the development of an organized flow field with well-defined spatial velocity gradients. A flow field characterized by a Gaussian covariance would tend to have smaller spatial velocity gradients (and weaker convective accelerations) than a flow field described by an exponential model with similar parameter values.

For each hydraulic quantity at each discharge, we estimated covariance model parameters through a three-stage process. We first examined the experimental semivariogram to assess whether a Gaussian or exponential model would be more appropriate and whether a nugget effect would be necessary, obtained initial parameter estimates using an interactive graphical routine, and then optimized the model parameters with an iterative computational algorithm that minimized the weighted sum of squared differences between the experimental $\widehat{\gamma}(\mathbf{h}_k)$ and model $\gamma(\mathbf{h}_k)$ semivariogram values

$$WSS = \sum_{k=1}^{K} \frac{N(\mathbf{h}_k)}{\gamma(\mathbf{h}_k)} \left[\widehat{\gamma}(\mathbf{h}_k) - \gamma(\mathbf{h}_k)\right]. \tag{5}$$

The weighting factor in this expression is an approximation for the variance of semivariogram estimates that assigns more weight to shorter lags having a larger number of pairs of observations (Cressie, 1985). In some cases with large nugget effects and poorly defined spatial structure, models fit by the automated weighted least squares procedure were clearly inferior to those parameterized by eye and we retained our initial parameter estimates.

We used a second geostatistical metric, the cross-correlogram, to quantify spatial covariance between pairs of hydraulic quantities at different scales. Following Goovaerts (1997), we computed the cross-covariance between two random variables z_i and z_j located at opposite ends of the vector $\mathbf{h}$ as

$$C_{ij}(\mathbf{h}) = \frac{1}{N(\mathbf{h})} \sum_{\alpha=1}^{N(\mathbf{h})} z_i(s_\alpha) \cdot z_j(s_\alpha + \mathbf{h}) - m_{i,-\mathbf{h}} \cdot m_{j,+\mathbf{h}}, \tag{6}$$

where $m_{i,-\mathbf{h}} = \frac{1}{N(\mathbf{h})} \sum_{\alpha=1}^{N(\mathbf{h})} z_i(s_\alpha)$ and $m_{j,+\mathbf{h}} = \frac{1}{N(\mathbf{h})} \sum_{\alpha=1}^{N(\mathbf{h})} z_j(s_\alpha + \mathbf{h})$ are the means of the z_i values at the tail of $\mathbf{h}$ and the z_j values at the head of $\mathbf{h}$, respectively. Because values of $C_{ij}(\mathbf{h})$ depend on the magnitudes of z_i and z_j, which could have different scales, we used the cross-correlogram to obtain a more readily interpretable, bounded measure of spatial cross-correlation:

$$\rho_{ij}(\mathbf{h}) = \frac{C_{ij}(\mathbf{h})}{\sqrt{\sigma^2_{i,-\mathbf{h}} \cdot \sigma^2_{j,+\mathbf{h}}}} \in [-1, +1], \tag{7}$$

where $\sigma^2_{i,-\mathbf{h}} = \frac{1}{N(\mathbf{h})} \sum_{\alpha=1}^{N(\mathbf{h})} [z_i(s_\alpha) - m_{i,-\mathbf{h}}]^2$ and $\sigma^2_{j,+\mathbf{h}} = \frac{1}{N(\mathbf{h})} \sum_{\alpha=1}^{N(\mathbf{h})} [z_j(s_\alpha + \mathbf{h}) - m_{j,+\mathbf{h}}]^2$ are the variances of the tail z_i and head z_j values, respectively. We calculated experimental cross-correlograms for numerous combinations of hydraulic quantities but focus here on quantifying the spatial cross-correlation among mean velocities and turbulence intensities and local relative roughness values. Parametric modeling of cross-covariances is significantly more involved than for auto-covariances and is beyond the scope of this study.

2.4 Graphical representation

To emphasize interactions among the flow field and the bed topography and roughness elements, our velocity measurements are represented as proportional symbols overlain on a contour map of the channel (the minimum surveyed bed elevation was set to zero and serves as our vertical datum). To facilitate direct comparison among different flow stages, the distributions of measured values for each variable were pooled over the three discharges and the deciles of this aggregate distribution were used as class breaks. The sizes (areas) of the point symbols for each of these decile classes were determined by assigning the first decile to the smallest of a fixed range of symbol sizes, the tenth decile to the largest, and then linearly scaling the symbol sizes (areas) for the intermediate deciles over this range. The sizes of the first and last symbols were thus fixed, but the sizes of the intermediate symbols varied from one map to the next depending on the shape of the distribution of the flow characteristic; for a given map, the area of a symbol remained proportional to the corresponding decile value. The colors of each symbol class were also assigned based on these deciles, grading from pure red for the first decile to pure blue for the tenth decile. Locations with low values of the flow characteristic are thus represented as small, red circles, and as flow strength increases the point symbol becomes larger and more blue. In addition to plan view maps, the corresponding histograms of each flow characteristic are also presented on the right side of Figures 3 - 8. These plots are normalized to be true density histograms (i.e., the area of the bars sums to unity) rather than frequency histograms (i.e., counts of observations in each bin) so that the distributions can be compared directly in spite of the different sample sizes.

3 Results

3.1 Effects of flow stage on distributions of velocity and turbulence intensity

Figures 3 - 8 illustrate the spatial patterns and probability distributions of each flow characteristic at each discharge. To assess whether the shape and/or position (median) of these distributions changed from one discharge to another for a given flow characteristic, we performed Kolmogorov-Smirnov (KS) two-sample tests of independence (Rhoads et al., 2003). The test statistic for this non-parametric test is the maximum absolute difference between two cumulative distributions, which is compared to the greatest absolute difference expected to occur by chance under the null hypothesis that the samples were drawn from the same distribution. The results of the eighteen KS tests we performed (three for each of the six flow characteristics) are presented in Table 6, where a p-value < 0.05 indicates that the distributions of the flow characteristic at the indicated pair of discharges were statistically significantly different from one another.

The distributions of mean streamwise velocity U/U_* shown in Figure 3 were similar across the three discharges, with highly non-significant KS test p-values. The median U/U_* increased slightly from the second to third discharge, but the variance and shape of the probability distributions changed little. The primary effect of increasing flow stage on the spatial distribution of U/U_* was the inundation of the shallow bench on the right side of the channel (transverse distances greater than 9 m from the left bank). At 1.13 m^3/s, much of this high-roughness zone was exposed, with low velocities recorded along the area of slightly deeper flow at the far right [from (s,n) coordinates (0, 15) to (6, 12), in meters]. At the intermediate discharge of 2.41 m^3/s, moderate streamwise velocities were measured along this bench and toward the left bank due to the increase in stage. The flow pattern through the thalweg at this discharge was not well-defined because several of our measurements in this area were discarded due to poor data quality at $0.2h$. Very low and even negative (upstream-directed) U/U_* were observed in the lee of the large boulder at (4.5, 9). At the highest discharge, flow was concentrated in the main thalweg angling downstream to the left from the channel centerline [(0, 8) to (4.5, 5)], but a second, parallel area of higher U/U_* also developed on the bench to the right [(0, 14) to (4.5, 13)].

A more interesting pattern was observed for the mean vertical velocity V/U_* (Figure 4). The spatial arrangement and probability distribution of V/U_* were quite similar for the low and intermediate discharges, with upwelling flow (positive V/U_*) within the main thalweg and either slightly downwelling or negligible vertical velocities along its margin. A few large values of V/U_* were also observed in association with large roughness elements on the right bench [e.g., at (4.5, 14) at 2.41 m^3/s]. At the highest discharge, however, the distribution of V/U_* changed significantly as flow in the thalweg began downwelling, most noticeably at cross-section 2 where depth increased abruptly [(1.5, 3) to (1.5, 10)]. At all three discharges, we observed downwelling upstream of the large boulder [(3, 9)] and upwelling on its left side toward the thalweg [(4.5, 9)].

Our measurements of the transverse component of the mean velocity W/U_* are summarized in Figure 5 and indicate strong stage-dependence. The change in the probability distribution of W/U_* from 1.13 to 2.41 m^3/s was not quite statistically significant, but an increase in transverse flow toward the left bank (positive W/U_*) was evident in cross-sections 1 and 2 both within the thalweg on the left [e.g., (1.5, 5)] and, at 2.41 m^3/s, on the shallow bench at river right [e.g., (1.5, 10)]. As stage increased further at 3.25 m^3/s, a significant shift in the distribution of W/U_* to positive values (toward the left bank) occurred as transverse flow off of the right bench and into the thalweg [(0, 11) to (3, 8)] became more fully developed, although negligible to rightward transverse flow was measured at a few points in close proximity to protruding clasts [e.g., (1.5, 15)]. The mean transverse velocity component was directed toward the right along the left bank and in the thalweg at cross-section 4 as flow converged to the left of the large boulder at the lower end of the riffle.

Spatial distributions of turbulence intensity also exhibited stage-dependent spatial patterns. For the streamwise component u'/U_* (Figure 6), the KS test indicated that distributions at 1.13 and 2.41 m^3/s were significantly different, but the fact that differences between 1.13 and 3.25 m^3/s and 2.41 and 3.25 m^3/s were insignificant suggest that this result was an artifact of rejecting several of the 2.41 m^3/s measurements in the thalweg. In general, the spatial distribution of u'/U_* was quite similar to that of U/U_* and appeared to be primarily a function of flow depth, with more intense turbulence where depths and mean velocities were higher (Clifford, 1998). For the vertical component of turbulence illustrated in Figure 7, our data suggest a weaker relationship with depth and mean velocity. High values of v'/U_* tend not to correspond closely with V/U_* and some of the greatest intensities were observed in shallow water along the left bank [e.g, (6, 1)], which resulted in significantly different distributions for the low and intermediate discharges. The difference between the 1.13 m^3/s and 3.25 m^3/s distributions was highly significant, with smaller mean and median values at the highest flow due to a reduced number of large values of v'/U_*, particularly in the thalweg. The spatial pattern and probability distribution of transverse turbulence intensity w'/U_* varied little among the three discharges (Figure 8), with essentially no change in the mean or median. The primary control on w'/U_* appeared to be the flow depth — intensities were greatest in the thalweg and smaller along the left bank and the shallow bench at right, where w'/U_* values increased with stage.

3.2 Geostatistical models of spatial structure

To summarize and quantify the spatial patterns illustrated in Figures 3 - 8, we calculated experimental semivariograms in the streamwise s and transverse n directions for each flow characteristic and summarized these spatial structures by fitting parametric covariance models. Semivariograms for mean velocity components and turbulence intensities are plotted in Figures 9 and 10, respectively, and the corresponding model parameters are listed in Table 7. Some important geostatistical caveats relating to sample design, the nugget effect, and parameter estimation must be considered in interpreting these results. The semivariogram value $\gamma(|\mathbf{h}|)$ at lag $|\mathbf{h}| = 0$ is zero by definition (Equation 1), and the nugget effect is expressed as a discontinuity at the origin such that $\gamma(\varepsilon) > 0$ for an arbitrarily small lag distance $|\mathbf{h}| = \varepsilon > 0$. This vertical offset is a consequence of measurement error and/or fine-scale variability due to processes operating over lag distances smaller than the most closely spaced observations of the sampling design (Oliver and Webster, 1986). These two contributions to the nugget cannot be distinguished unless co-located replicates are available to estimate the measurement error variance, and the most effective means of establishing the behavior near the origin is to increase the spatial resolution of the sampling design — that is, decreasing the smallest lag distance between measurement locations (Goovaerts, 1997). The sampling strategy used in this study thus failed to reveal any information on processes operating at distances less than 1.5 m in the s direction or less than 0.5 m in the n direction and we had to model the nugget effect by extrapolating the semivariogram for the first few lags back to the ordinate, which is the typical approach in geostatistical practice (Goovaerts, 1997). A related issue is that of automated parameter estimation by weighted least squares. A noisy experimental semivariogram could be fit with either a pure nugget effect or a covariance model with an extremely long range, and numerical fitting procedures often opt for the latter. In this case, $\gamma(\mathbf{h})$ increases only slightly over the sampled range of lags and, like the pure nugget model, indicates a lack of correlation at the spatial scales considered, though the process could be spatially structured at smaller and/or larger scales. For the purposes of this study, semivariograms modeled as either a pure nugget (by eye) or a long-range, high-sill covariance (by weighted least squares) can be interpreted as an indication that the time-averaged spatial structure of the flow characteristic is poorly defined between the length scales of 1.5 and 6 m and 0.5 and 10 m in the *s* and/or *n* directions, respectively.

For the mean streamwise velocity U/U_* (left column of Figure 9), the total sill (nugget + sill of the covariance model) of the *s* semivariogram decreased as discharge increased, with the largest change occurring between 1.13 and 2.41 m^3/s. At the lowest discharge, the shallow depth dictated that the flow field would be dominated by the localized effects of roughness elements, yielding a less smooth spatial structure characterized by a higher sill. In the *n* direction, the sill of the U/U_* semivariogram was lowest for the lowest discharge because fewer pairs of points are on opposite sides of the break in slope [(-1.5, 10) to (6, 9)] between the right bench, with very low velocities, and the thalweg, where velocities are higher. The short range of the 1.13 m^3/s semivariogram indicates that the transverse spatial structure was also rougher due to the greater influence of protuberant clasts at lower relative depths. The sills of the U/U_* semivariograms for 2.41 and 3.25 m^3/s were similar, but the greater range at 3.25 m^3/s indicated that the spatial structure of the flow field became smoother as stage increased and the effects of roughness diminished. The dip in $\widehat{\gamma}(\mathbf{h})$ values at intermediate transverse lags for 1.13 m^3/s was due to the large number of pairs of points with similar U/U_* values located on opposite sides of the 4 - 6 m wide thalweg. Similarly, the high $\widehat{\gamma}(\mathbf{h})$ values at longer *n* lags at the two higher discharges resulted from the pairing of low velocities on the right bench with high velocities in the thalweg.

The experimental semivariograms for the mean vertical velocity V/U_* were not as well-defined, particularly in the *n* direction (center column of Figure 9). The *s* semivariograms for the low and intermediate discharges exhibited more coherent spatial structures and higher sills than the 3.25

m^3/s semivariogram due to a greater number of high values of V/U_* at the downstream end of the thalweg at the two lower discharges. The sill for 3.25 m^3/s was also the lowest of the n semivariograms because of the well-defined, laterally extensive areas of downwelling most evident at cross-sections 2 and 4. Sills were higher for the two lower discharges because the V/U_* values of successive points along a cross-section were less regular, with strong upwelling often juxtaposed against relatively rapid downwelling over small lateral distances. These results suggest that the spatial structure of vertical velocity at lower flows was dominated by small-scale processes such as flow separation and eddy shedding associated with large roughness elements.

We observed strongly stage-dependent spatial patterns for the transverse component of the mean velocity (right column of Figure 9). In the s direction, the W/U_* experimental semivariogram increased steadily over the range of lag distances we sampled; the largest values of $\widehat{\gamma}(\mathbf{h})$ occurred at 2.41 m^3/s for intermediate lags and at 1.13 m^3/s for the greatest s lag of 6 m. These high semivariances reflected the contrast between left-directed flow at the upper end of the riffle and rightward velocities along the left bank and in the thalweg at cross-sections 4 and 5. At the highest discharge, the sill of the semivariogram was much lower because the rightward flow in the lower thalweg was not as strong and a continuous streamwise thread of moderate leftward velocities had formed on the right bench; the relative homogeneity of W/U_* values on the bench reduced the average squared difference at all s lags. In the transverse direction, the highest sill was observed at 2.41 m^3/s because strong right– and left–directed currents occurred along the same cross-section, most notably sections 3 and 5. The sill at 3.25 m^3/s was not as high because of the relatively uniform leftward flow off of the right bench and the weakening of the flow into the thalweg from the left bank. The lowest n direction sill occurred at the lowest discharge because absolute values of W/U_* vales were smaller on average and tended to be negative (rightward), with only a few positive (leftward) observations.

In general, the spatial structure of turbulence intensity was not as well-defined as for the mean velocity components, and the effects of flow stage were more difficult to discern from our measurements and analyses. The sill of the semivariogram for u'/U_* was lowest at the intermediate discharge for both the s and n directions and also appeared to have the most coherent spatial structure (left column of Figure 10). The high n-direction semivariances at the lowest discharge resulted from the juxtaposition of very low u'/U_* values on the right bench, where relative depths and mean velocities were lower, and moderate to high values in the thalweg along cross-sections 1 and 2. Similarly, the transverse sill at 3.25 m^3/s was higher than that for 2.41 m^3/s because a greater number of low u'/U_* values in shallow water were observed at the higher discharge. The sill of the v'/U_* semivariograms for both directions (center column of Figure 10) were highest at the intermediate discharge and lowest at the highest discharge and were influenced by the large number of high intensity observations made at 2.41 m^3/s along the left margin of the thalweg. The high transverse $\widehat{\gamma}(\mathbf{h})$ values at this discharge were due to the pairing of highly turbulent points on the left with areas of less-developed turbulence in the thalweg and on the shallow bench to the right. The contrast between the left and right margins of the channel was less pronounced at the highest discharge as the lateral distribution of v'/U_* became more homogeneous and reduced the sill of the n direction semivariogram. The streamwise spatial structure of transverse turbulence intensity was similar for the three discharges, but the effects of increasing flow stage were evident in the n direction (right column of Figure 10). The transverse sill of the w'/U_* semivariogram decreased with increasing discharge as the very low turbulence intensities along the right bench increased to create a more laterally homogeneous spatial distribution. These results suggest that turbulence became more intense and developed a more continuous spatial structure as stage increased and the localized effects of large roughness elements on the flow field became less pronounced.

3.3 Spatial analysis of the effects of local boundary roughness

We examined the local and lagged effects of boundary roughness on mean velocity components and turbulence intensities by computing cross-correlograms (Equation 7) between h/k_s, the local index of relative roughness described in Section 2.2, and each of the flow characteristics in Table 4. These results are illustrated in Figures 11 and 12, where the cross-correlation between h/k_s values at location $\mathbf{s}_\alpha$ and the specified flow characteristic at location $\mathbf{s}_\alpha + \mathbf{h}$ is plotted as a function of the lag $\mathbf{h}$ separating the observations; cross-correlograms were calculated for both the s and n directions. As opposed to the semivariograms discussed above, correlograms measure the similarity between lagged measurements, and a well-defined spatial structure is expressed as a smooth decrease in $\rho(\mathbf{h})$ with increasing lag. Because the cross-correlogram compares two different variables, the value of $\rho_{ij}(\mathbf{h})$ at lag zero is simply the correlation coefficient between co-located observations of the two variables; $\rho_{ij}(\mathbf{h})$ values for larger $\mathbf{h}$ quantify the spatial persistence of this correlation.

The cross-correlograms relating local boundary roughness h/k_s to the mean streamwise velocity U/U_* (left column of Figure 11) indicate a strongly stage-dependent effect of local boundary roughness on flow strength. The lag-zero cross-correlation between h/k_s and U/U_* was consistently positive and increased with discharge, indicating an increase in mean velocity as flow depth increased relative to the roughness height of the bed. This relationship was strongest at 3.25 m^3/s when depths and velocities were greatest and weakest at 1.13 m^3/s when h/k_s was smaller and the effects of roughness more pronounced. The decrease in $\rho_{ij}(\mathbf{h})$ from 0 to the first s lag for the two highest discharges indicated that the effects of roughness diminished, on average, within a streamwise distance of 1.5 m, but the cross-correlogram increased again for the next lag and no clearly-defined spatial structure was evident. A more coherent pattern emerged in the n direction, where $\rho_{ij}(\mathbf{h})$ decreased steadily over the first three lags at all three discharges while preserving the trend of increasing correlation with increasing discharge over this range. The transverse spatial cross-correlation between h/k_s and U/U_* was most persistent at the highest measured discharge, suggesting that the flow became more spatially coherent as stage increased and drowned out roughness elements on the right bench. At 1.13 m^3/s, the rapid decline to negative correlations and strong negative correlations at lags from 2-5 m was primarily due to the pairing of small h/k_s values on both margins of the thalweg with high velocities in the thalweg proper.

For the vertical component of mean velocity, lag-zero correlations between h/k_s and V/U_* were positive but neither as strong nor as clearly stage-dependent as for U/U_* (center column of Figure 11). The highest value of $\rho_{ij}(\mathbf{0})$ occurred at 2.41 m^3/s but the correlations for 1.13 and 3.25 m^3/s were essentially identical. The correlation at the intermediate discharge was higher due to the upwelling (large positive V/U_*) that developed in the deeper flow in the thalweg, where h/k_s was also greatest. Neither the streamwise nor transverse spatial structure was well-developed for any of the three discharges. The erratic behavior of the h/k_s, V/U_* n-direction cross-correlogram at 1.13 m^3/s could have been an expression of very localized interactions among vertical velocities and individual clasts as flow separated and eddies were shed, but outlying observations of either variable also could have influenced these $\rho_{ij}(\mathbf{h})$ values.

The lag-zero correlation between h/k_s and the mean transverse velocity was negligible at 1.13 m^3/s and weakly negative at the two higher discharges. For the s direction cross-correlograms, the most notable trend was the highly negative $\rho_{ij}(\mathbf{h})$ values for the three greatest lags at 2.41 m^3/s as a result of the large number of negative values of W/U_* (rightward flow) in cross-section 5 paired with moderate to high h/k_s values at the upper end of the thalweg. In the n direction, the 1.13 m^3/s cross-correlogram was quite erratic, but a parabolic trend with negative correlations at the smallest and largest lags and positive correlations at intermediate distances was evident for the higher discharges. Referring back to the maps in Figure 5 indicated that this trend could be explained by rightward flow (negative W/U_*) and high h/k_s in the thalweg producing negative values of $\rho_{ij}(\mathbf{h})$ for small $\mathbf{h}$ and positive $\rho_{ij}(\mathbf{h})$ at larger $\mathbf{h}$ as the negative W/U_* values in the thalweg were paired with points having greater roughness (lower h/k_s) on the right bench; at greater lags from 8-10 m, the correlation declined again and approached zero as more pairs of points combined relatively high and low values of both variables.

Cross-correlograms relating local boundary roughness to turbulence intensity tended to be irregular over the range of lag distances covered by our sample design (Figure 12), but the lag-zero correlations yielded some insight into the effects of stage and roughness on turbulence components. u'/U_* and w'/U_* were uncorrelated with h/k_s at lag zero for the lowest discharge and positively correlated at the two higher discharges, suggesting that, at a point, these two components of turbulence intensity increased with flow depth relative to boundary roughness. For v'/U_*, $\rho_{ij}(\mathbf{0})$ was lower but still positive for the two highest flows and moderately negative at 1.13 m^3/s, suggesting that vertical eddying could be slightly enhanced where roughness elements occupied a greater proportion of the flow depth. The only clear trend that emerged at greater streamwise lags occurred at the lowest discharge, when $\rho_{ij}(\mathbf{h})$ decreased over the first three lags for all three intensity components, going from positive to negative over this 3 m distance for v'/U_*. This result could suggest that at low stages when the effects of boundary roughness are most pronounced, turbulence intensity lags behind the roughness and tends to peak downstream from points of high h/k_s where flow reattaches in the lee of obstacles and greater flow depths (and mean velocities) allow larger-scale eddies to develop. In the n direction, the cross-correlation between h/k_s and each of the three intensity components at 2.41 m^3/s decreased over the first three lags and became negative by a transverse lag distance of 1.5 m. In reference to Figure 5, this trend could be a consequence of the well-developed transverse flow at this discharge, to the left at the upper two cross-sections and to the right at the lower two cross-sections. The interaction of these lateral currents with roughness elements could have produced delayed, negative peaks in $\rho_{ij}(\mathbf{h})$ (i.e., high values of u'/U_*, v'/U_*, and/or w'/U_* located to the side of low values of h/k_s, especially on the right bench) where this transverse flow reattaches in the (lateral) lee of obstacles.

3.4 Thalweg vertical profiles

In addition to the cross-sectional deployment upon which our analysis of plan view spatial patterns was based, we also measured five thalweg vertical profiles to resolve salient features of three-dimensional flow structure. These data are presented in Figures 13 and 14, along with longitudinal profiles of local roughness height k_s and bed elevation. Our ADV data pre-processing (Section 2.1) resulted in the rejection of a number of measurement points, most notably at greater depths, due to the difficulty of obtaining reliable velocity measurements near the bed, and/or near the water surface at higher discharges, due to aeration, and limited our ability to resolve the shape of certain profiles. Visual inspection of these profiles suggested that some observations (i.e., the top measurement at cross-section 1 and the bottom measurement at cross-section 3 at 3.25 m^3/s) that satisfied our filtering criteria might have been of dubious quality as well.

Despite the limitations of our data set, the thalweg profiles, together with the plan view maps in Figures 3 - 8, revealed important aspects of the three-dimensional flow structure through the riffle. Scaling the mean velocity components and turbulence intensities by the reach-averaged friction velocity U_* effectively collapsed profiles measured at different discharges about a common trend by accounting for the increase in depth-averaged velocity with depth. For the streamwise component, differences between discharges were most pronounced in the third and fourth profiles. At cross-section 4, where the flow field was affected by the rise in the bed elevation profile at 3.5 m, U/U_* was highest at the intermediate discharge, with the greatest difference at the bottom of the profile. The vertical and lateral components of the mean velocity varied more along the thalweg and among the three discharges in response to stage-dependent secondary currents. At the first cross-section, V/U_* was negligible to slightly negative (downwelling) at the low and intermediate discharges while W/U_* was slightly positive, indicating weak leftward flow. As the discharge increased to 3.25 m^3/s, strong upwelling developed above 0.3h and transverse velocities near the top of the profile also increased. For the next profile downstream, lateral flow toward the left bank was more pronounced at all three discharges, and strong downwelling developed in the upper half of the profile at 2.41 and 3.25 m^3/s as flow converged and descended into the thalweg. For the third profile, this downwelling motion was less developed at 1.13 and 2.41 m^3/s but remained strong at the highest flow. High transverse velocities toward the right bank (negative W/U_*) were also measured in the middle of the profile at 3.25 m^3/s but became weaker toward the surface; a similar pattern of rightward flow at depth and leftward flow at the surface was observed at the low and intermediate discharges. At cross-section 4, V/U_* fluctuated slightly about zero at 2.41 and 3.25 m^3/s but weak upwelling occurred at the lowest discharge; W/U was negative (rightward) at all depths and discharges at this location as flow converged off of the left bank into the thalweg. This rightward flow was well-developed at all discharges at cross-section 5, though the lateral current became weaker toward the top of the profile at the two higher discharges. Predominantly positive values of V/U_* at the intermediate discharge and negative values at the highest flow suggest that the vertical component of the mean velocity switched from upwelling to downwelling between 2.41 and 3.25 m^3/s. Coupled with the maps of V/U_* and W/U_* in Figures 4 and 5, these profiles indicate a zone of convergence with leftward, downwelling flow at the upstream end of the thalweg that was most clearly developed at 3.25 m^3/s and an opposite pattern of rightward, upwelling flow at the lower end of the riffle that was best expressed at the intermediate discharge.

The profiles in Figure 14 indicate that turbulence intensities for the three discharges were similar when scaled by the reach-averaged friction velocity. For the streamwise component, u'/U_* generally decreased away from the boundary as U/U_* increased. A similar pattern of decreasing turbulence intensity with increasing distance from the bed was also apparent in the v'/U_* profiles, but w'/U_* tended to be more uniform over the flow depth. Closer scrutiny of the mean velocity and turbulence intensity profiles indicated that subtle peaks in v'/U_* and/or w'/U_* tended to occur at vertical locations where V/U_* and/or W/U_* changed sign (i.e., transitions from leftward to rightward and/or upwelling to downwelling flow) over a small vertical distance, indicating flow separation. Profile 5 provided the best illustration of this relationship, where the peak in v'/U_*

at $0.3h$ for 2.41 and 3.25 m^3/s corresponded to a change from weakly upwelling to strong downwelling in the vertical profile of V/U_*. Similarly, the spike in w'/U_* at $0.3h$ observed for all three discharges was associated with a transition from negligible lateral flow at $0.2h$ to a strong rightward current at $0.3h$.

4 Discussion and conclusion

Our extensive, high-resolution measurements of flow velocity and bed topography and spatially explicit statistical analyses of these data provided detailed information on reach-scale, three-dimensional flow characteristics in a steep, cobble-bed riffle. Collecting data at three discharges also provided quantitative insight on the effects of stage and roughness on the spatial variability of these flow fields. Although the relative simplicity of our instrumentation and deployment strategy did not allow us to directly examine the coherent flow structures emphasized by Roy and colleagues over the past decade (Robert et al., 1993; Roy, Buffin-Belanger and Deland, 1996; Ferguson et al., 1996; Buffin-Belanger and Roy, 1998; Roy et al., 1999; Buffin-Belanger et al., 2000; Roy et al., 2004; Lamarre and Roy, 2005), our study complements previous research by 1) extending this type of investigation to a higher-gradient, coarser-grained fluvial system; 2) incorporating measurements of lateral velocity; 3) introducing a geostatistical framework for quantifying spatial variability; and 4) providing a more thorough, spatially distributed perspective on the time-averaged mean and turbulent flow characteristics and their relationship with boundary roughness at the reach scale.

Our study is most similar to that of Lamarre and Roy (2005), who found that complex bed topography and protuberant clasts had only minor impacts on the flow field in a moderate-gradient (0.002) gravel-bed ($D_{84} = 100$ mm) gravel-bed river, and our results support several of their conclusions. In general, our measurements and analyses indicate that even in a cobble-bed riffle where D_{84} was of the same order as the mean depth (Tables 1 and 3), flow patterns were controlled by the gross morphology of the channel and thus exhibited a reasonable degree of organization, particularly at the two highest discharges we sampled. At these stages, individual roughness elements exerted less of an influence on the flow field as well-defined secondary currents developed in response to the more salient topographic features of the channel. While our data do not allow us to address the length or time scales of coherent flow structures in the sense of Roy et al. (2004), our observations over a range of discharges lend support to their conclusion that flow depth is the fundamental control on flow structure; both the strength and spatial persistence of the flow increased at higher stages. These effects were expressed most clearly in the streamwise semivariograms of mean streamwise velocity (top left panel of Figure 9), where sills decreased as discharge increased and the spatial structure of the flow became smoother and more continuous. Cross-correlograms relating local boundary roughness to mean and turbulent flow characteristics provided further evidence of the importance of flow depth relative to roughness height as a control on both the magnitude of the mean velocity vector and the intensity of turbulence, although the generally rapid decline in correlation with increasing lag suggested that the effects of roughness were quite localized. These results are consistent with the finding of Lamarre and Roy (2005) that the influence of individual clasts or bedforms was only expressed in velocity profiles over distances less than $25D_{84}$ (≈ 2.5 m in their study). Thus, while the flow field does bear the imprint of topographic variability at high spatial frequencies, most noticeably at lower discharges, overall flow patterns primarily express the lower-frequency, bulk morphology of the channel. Our observations over a relatively small range of low to moderate discharges also suggest that the noise introduced to the flow field by high-frequency topography is increasingly drowned out as stage rises; Whiting (1997) reported a similar result from a smaller, finer-grained channel. Additional field data collected over a range of discharges with vertical arrays of synchronized, high-frequency current meters are needed to assess the stage-dependence of turbulent flow structures in more detail.

The spatially explicit, stochastic approach adopted in this study provided an effective means of summarizing our observations and informing our interpretations. Scaling our velocity and turbulence intensity measurements by the reach-averaged friction velocity for each discharge allowed us to directly compare the variability and spatial patterns of the three flow fields by accounting for differences in the mean depth. Although statistical tests comparing the distributions of each flow characteristic at the three discharges yielded some insight (Table 6), important information would have been lost had we not considered the spatial context of our measurements. For example, differences among the probability distributions of U/U_* for the three discharges were highly non-significant, suggesting no stage dependence of the mean streamwise velocity. The semivariograms in Figure 9, however, revealed that the spatial structure of U/U_* varied as a function of stage, in both the streamwise and transverse directions. In many cases, careful scrutiny of empirical semivariograms, together with proportional symbol maps of flow characteristics overlain on the bed topography, directed our attention to certain aspects of the flow field and its interaction with the boundary and helped us gain a more detailed understanding of hydraulic patterns within the riffle. We suggest that incorporating spatial information via geostatistical methods could enrich Lamouroux's (1995; 1998) stochastic hydraulic framework and facilitate inter-site (e.g., Rhoads et al., 2003) or (in our case) inter-stage comparisons. Just as Lamouroux et al. (1995) developed functional relationships between basic geomorphic variables and parameters describing probability distributions of velocity, parameters describing the spatial covariance structure of mean and turbulent flow characteristics could be linked to other, more easily measured, channel properties such as width, depth, slope, and sediment grain size. In addition to yielding fundamental insight as to the factors controlling the spatial variability of velocity and turbulence intensity, such an approach could be used in a more applied context to estimate these flow characteristics from more readily available data. Our ongoing research focuses on identifying these controls and linking our empirical observations and geostatistical descriptions to fluid mechanical processes.

Acknowledgements

We are grateful to Jason Emmanuel, Julie Holcombe, Jessica Kuzma, and Debbie Zarnt for their invaluable field assistance, and to Phaedon Kyriakidis for helping us develop the code for our geostatistical analyses. We would also like to thank the Nature Conservancy for access to their Phantom Canyon Preserve and the USDA Forest Service for their financial support. The lead author's participation on this project began through the NSF Research Experience for Undergraduates Program at Colorado State University, and he has also received financial support from the American Society for Engineering Education. The helpful suggestions offered by Hélène Lamarre, Anne Chin, and an anonymous reviewer resulted in significant improvements to our initial manuscript.

References

Babaeyan-Koopaei, K., Ervine, D. A., Carling, P. A. and Cao, Z., 2002. Velocity and turbulence measurements for two overbank flow events in River Severn. Journal of Hydraulic Engineering-ASCE 128(10), 891–900.

Best, J. L., 1993. On the interactions between turbulent flow structure, sediment transport, and bedform development: some considerations from recent experimental research. Clifford, N. J., French, J. R., and Hardistry, J. (Eds.), Turbulence: Perspectives on Flow and Sediment Transport. John Wiley and Sons, New York, pp. 61–92.

Biron, P. M., Lane, S. N., Roy, A. G., Bradbrook, K. F. and Richards, K. S., 1998. Sensitivity of bed shear stress estimated from vertical velocity profiles: The problem of sampling resolution. Earth Surface Processes and Landforms 23(2), 133–139.

Booker, D. J., Sear, D. A. and Payne, A. J., 2001. Modelling three-dimensional flow structures and patterns of boundary shear stress in a natural pool-riffle sequence. Earth Surface Processes and Landforms 26(5), 553–576.

Buffin-Belanger, T. and Roy, A. G., 1998. Effects of a pebble cluster on the turbulent structure of a depth-limited flow in a gravel-bed river. Geomorphology 25(3-4), 249–267.

Buffin-Belanger, T., Roy, A. G. and Kirkbride, A. D., 2000. On large-scale flow structures in a gravel-bed river. Geomorphology 32(3-4), 417–435.

Byrd, T. C., Furbish, D. J. and Warburton, J., 2000. Estimating depth-averaged velocities in rough channels. Earth Surface Processes and Landforms 25(2), 167–173.

Chappell, A., Heritage, G. L., Fuller, I. C., Large, A. R. G. and Milan, D. J., 2003. Geostatistical analysis of ground-survey elevation data to elucidate spatial and temporal river channel change. Earth Surface Processes and Landforms 28(4), 349–370.

Clifford, N. J., 1996. Morphology and stage-dependent flow structure in a gravel-bed river. Ashworth, P. J., Bennett, S. J., Best, J. L., and McLelland, S. J. (Eds.), Coherent Flow Structures in Open Channels. John Wiley and Sons Ltd, Chichester, pp. 545–566.

Clifford, N. J., 1998. A comparison of flow intensities in alluvial rivers: Characteristics and implications for modelling flow processes. Earth Surface Processes and Landforms 23(2), 109–121.

Clifford, N. J. and French, J. R., 1993a. Monitoring and analysis of turbulence in geophysical boundaries: some analytical and conceptual issues. Clifford, N. J., French, J. R., and Hardistry, J. (Eds.), Turbulence: Perspectives on Flow and Sediment Transport. John Wiley and Sons, New York, pp. 93–120.

Clifford, N. J. and French, J. R., 1993b. Monitoring and modelling turbulent flow: historical and contemporary perspectives. Clifford, N. J., French, J. R., and Hardistry, J. (Eds.), Turbulence: Perspectives on Flow and Sediment Transport. John Wiley and Sons, New York, pp. 1–34.

Clifford, N. J., Robert, A. and Richards, K. S., 1992. Estimation of flow resistance in gravel-bedded rivers - a physical explanation of the multiplier of roughness length. Earth Surface Processes and Landforms 17(2), 111–126.

Cressie, N., 1985. Fitting variogram models by weighted least-squares. Journal of the International Association for Mathematical Geology 17(5), 563–586.

Deutsch, C. V. and Journel, A. G., 1998. GSLIB: Geostatistical Software Library. Oxford University Press, New York.

Ferguson, R., Kirkbride, A. D. and Roy, A. G., 1996. Markov analysis of velocity fluctuations in gravel-bed rivers. Ashworth, P. J., Bennett, S. J., Best, J. L., and McLelland, S. J. (Eds.), Coherent Flow Structures in Open Channels, John Wiley and Sons, New York, pp. 165–183.

Finelli, C. M., Hart, D. D. and Fonseca, D. M., 1999. Evaluating the spatial resolution of an acoustic Doppler velocimeter and the consequences for measuring near-bed flows. Limnology and Oceanography 44(7), 1793–1801.

Goovaerts, P., 1997. Geostatistics for Natural Resource Evaluation. Oxford University Press, New York.

Goring, D. G. and Nikora, V. I., 2002. Despiking acoustic Doppler velocimeter data. Journal of Hydraulic Engineering-ASCE 128(1), 117–126.

Kirkbride, A., 1993. Observations of the influence of bed roughness on turbulence structure in depth limited flows over gravel beds. Clifford, N. J., French, J. R., and Hardistry, J. (Eds.), Turbulence: Perspectives on Flow and Sediment Transport, John Wiley and Sons, New York, pp. 185–196.

Lamarre, H. and Roy, A. G., 2005. Reach scale variability of turbulent flow characteristics in a gravel-bed river. Geomorphology 68(1-2), 95–113.

Lamouroux, N., 1998. Depth probability distributions in stream reaches. Journal of Hydraulic Engineering-ASCE 124(2), 224–227.

Lamouroux, N., Souchon, Y. and Herouin, E., 1995. Predicting velocity frequency-distributions in stream reaches. Water Resources Research 31(9), 2367–2375.

Lane, S. N., 2005. Roughness - time for a re-evaluation? Earth Surface Processes and Landforms 30(2), 251–253.

Lane, S. N., Biron, P. M., Bradbrook, K. F., Butler, J. B., Chandler, J. H., Crowell, M. D., McLelland, S. J., Richards, K. S. and Roy, A. G., 1998. Three-dimensional measurement of river channel flow processes using acoustic Doppler velocimetry. Earth Surface Processes and Landforms 23(13), 1247–1267.

Lawless, M. and Robert, A., 2001a. Scales of boundary resistance in coarse-grained channels: turbulent velocity profiles and implications. Geomorphology 39(3-4), 221–238.

Lawless, M. and Robert, A., 2001b. Three-dimensional flow structure around small-scale bedforms in a simulated gravel-bed environment. Earth Surface Processes and Landforms 26(5), 507–522.

McBratney, A. B. and Webster, R., 1986. Choosing functions for semi-variograms of soil properties and fitting them to sampling estimates. Journal of Soil Science 37(4), 617–639.

McLelland, S. J. and Nicholas, A. P., 2000. A new method for evaluating errors in high-frequency ADV measurements. Hydrological Processes 14(2), 351–366.

Nezu, I. and Nakagawa, H., 1993. Turbulence in Open-Channel Flows. IAHR Monograph Series. A.A. Balkema, Rotterdam.

Nikora, V. I., Goring, D. G. and Biggs, B. J. F., 1998. On gravel-bed roughness characterization. Water Resources Research 34(3), 517–527.

Nikora, V. I. and Smart, G. M., 1997. Turbulence characteristics of New Zealand gravel-bed rivers. Journal of Hydraulic Engineering-ASCE 123(9), 764–773.

Oliver, M. A. and Webster, R., 1986. Semi-variograms for modeling the spatial pattern of landform and soil properties. Earth Surface Processes and Landforms 11(5), 491–504.

Rhoads, B. L., Schwartz, J. S. and Porter, S., 2003. Stream geomorphology, bank vegetation, and three-dimensional habitat hydraulics for fish in midwestern agricultural streams. Water Resources Research, 39(8), 1218, doi:10.1029/2003WR002294.

Robert, A. and Richards, K. S., 1988. On the modeling of sand bedforms using the semivariogram. Earth Surface Processes and Landforms 13(5), 459–473.

Robert, A., Roy, A. G. and DeSerres, B., 1993. Space-time correlations of velocity measurements at a roughness transition in a gravel-bed river. Clifford, N. J., French, J. R., and Hardistry, J. (Eds.), Turbulence: Perspectives on Flow and Sediment Transport, John Wiley and Sons, New York, pp. 165–183.

Robert, A., Roy, A. G. and DeSerres, B., 1996. Turbulence at a roughness transition in a depth limited flow over a gravel bed. Geomorphology 16(2), 175–187.

Rodriguez, A., Sanchez-Arcilla, A., Redondo, J. M. and Mosso, C., 1999. Macroturbulence measurements with electromagnetic and ultrasonic sensors: a comparison under high-turbulent flows. Experiments in Fluids 27(1), 31–42.

Roy, A. G., Biron, P. and DeSerres, B., 1996. On the necessity of applying a rotation to instantaneous velocity measurements in river flows. Earth Surface Processes and Landforms 21(9), 817–827.

Roy, A. G., Biron, P. M., Buffin-Belanger, T. and Levasseur, M., 1999. Combined visual and quantitative techniques in the study of natural turbulent flows. Water Resources Research 35(3), 871–877.

Roy, A. G., Buffin-Belanger, T. and Deland, S., 1996. Scales of turbulent coherent flow structures in a gravel-bed river. Ashworth, P. J., Bennett, S. J., Best, J. L., and McLelland, S. J. (Eds.), Coherent Flow Structures in Open Channels, John Wiley and Sons, New York, pp. 145–164.

Roy, A. G., Buffin-Belanger, T., Lamarre, H. and Kirkbride, A. D., 2004. Size, shape and dynamics of large-scale turbulent flow structures in a gravel-bed river. Journal of Fluid Mechanics 500, 1–27.

Shvidchenko, A. B. and Pender, G., 2001. Macroturbulent structure of open-channel flow over gravel beds. Water Resources Research 37(3), 709–719.

Smart, G. M., 1994. Turbulent velocities in a mountain river. Cotroneo, G. , and Rumer, R. (Eds.), Hydraulic Engineering ’94, Vol. 2, American Society of Civil Engineers, New York, pp. 844–848.

Smith, J. D. and McLean, S. R., 1984. A model for flow in meandering streams. Water Resources Research 20(9), 1301–1315.

SonTek, 2000. FlowTracker Handheld ADV Technical Documentation, SonTek, San Diego.

Soulsby, R. L., 1980. Selecting record length and digitization rate for near-bed turbulence measurements. Journal of Physical Oceanography 10(2), 208–219.

Stewardson, M. J. and McMahon, T. A., 2002. A stochastic model of hydraulic variations within stream channels. Water Resources Research 38(1), 1007.

Voulgaris, G. and Trowbridge, J. H., 1998. Evaluation of the acoustic Doppler velocimeter (ADV) for turbulence measurements. Journal of Atmospheric and Oceanic Technology 15(1), 272–289.

Wackernagel, H., 2003. Multivariate Geostatistics, Springer-Verlag, Berlin.

Whiting, P. J., 1997. The effect of stage on flow and components of the local force balance. Earth Surface Processes and Landforms 22(6), 517–530.

Whiting, P. J., 2003. Flow measurement and characterization. Kondolf, M. , and Piégay, H. (Eds.), Tools in Fluvial Geomorphology, John Wiley and Sons, Chichester, UK, pp. 323–346.

Whiting, P. J. and Dietrich, W. E., 1991. Convective accelerations and boundary shear-stress over a channel bar. Water Resources Research 27(5), 783–796.

Wiberg, P. L. and Smith, J. D., 1991. Velocity distribution and bed roughness in high-gradient streams. Water Resources Research 27(5), 825–838.

Wohl, E. and Legleiter, C. J., 2003. Controls on pool characteristics along a resistant-boundary channel. Journal of Geology 111(1), 103–114.

Wu, F.-C. and Yang, K.-H., 2004. Entrainment probabilities of mixed-size sediment incorporating near-bed coherent flow structures. Journal of Hydraulic Engineering 130(12), 1187–1197.

Tables

Table 1: Hydraulic characteristics at measured discharges Q; $\bar{h}$ denotes the reach-averaged depth, U_* is the friction velocity, and D_{84} represents the intermediate clast diamter for which 84% of sampled grains are finer

Q (m^3/s)	$\bar{h}$ (cm)	U_* (cm/s)	$\bar{h}/D_{84}$
1.13	22.5	30.1	0.896
2.41	28.9	34.1	1.15
3.25	31.9	35.8	1.27

Table 2: Summary of data collection at each discharge

Q (m^3/s)	1.13	2.41	3.25
Depth-averaged cross-sectional data points	81	122	106
Depth-averaged cross-sectional data points rejected	13	24	9
thalweg profile data points rejected (of 40)	5	8	8

Table 3: Bed surface grain size distribution (mm)

D_5	D_{16}	D_{50}	D_{84}	D_{95}
17	51	124	251	437

Table 4: Notation for velocity components, after Nezu & Nakagawa (1993); friction velocity denoted by U_*

Direction	Downstream	Vertical	Cross-stream
Coordinate	s	z	n
Time-averaged mean velocity (cm/s)	U	V	W
Fluctuating velocity (cm/s)	u	v	w
Turbulence intensity (root mean square velocity; cm/s)	u'	v'	w'
Non-dimensional mean velocity	U/U_*	V/U_*	W/U_*
Non-dimensional turbulence intensity	u'/U_*	v'/U_*	w'/U_*

Table 5: Specifications for directional semivariograms

Direction	Streamwise (s)	Transverse (n)
Start lag distance (m)	0	0
Lag increment (m)	1.5	0.5
Maximum lag (m)	6	10
Azimuth (degrees)	90	0
Azimuth tolerance (degrees)	15	15
Horizontal band width (m)	5	3

Table 6: Kolmogorov-Smirnov test results for the six hydraulic quantities at the three discharges. The first number is the maximum absolute difference between the two cumulative probability distributions (percent) and the second number is the corresponding p-value. p-values less than 0.05 indicate that distributions of the hydraulic quantity at the two discharges are significantly different from one another.

	Discharge pair (m^3/s)		
	1.13, 2.41	1.13, 3.25	2.41, 3.25
U/U_*	8.43, 0.9269	10.28, 0.7700	8.88, 0.8194
V/U_*	9.66, 0.8287	25.86, 0.0075	26.12, 0.0020
W/U_*	19.42, 0.0848	34.79, 0.0001	19.99, 0.0347
u'/U_*	22.45, 0.0293	18.18, 0.1268	10.97, 0.5754
v'/U_*	28.81, 0.0019	32.19, 0.0004	8.49, 0.8586
w'/U_*	8.13, 0.9444	14.52, 0.3421	10.98, 0.5741

Table 7: Semivariogram model parameters for each flow characteristic at each discharge. C_{exp} and C_{Gauss} refer to the exponential and Gaussian covariance models described in the text.

Flow characteristic	Model parameters	Streamwise direction (s)			Transverse direction (n)		
		Discharge (m^3/s)					
		1.13	2.41	3.25	1.13	2.41	3.25
U/U_*	nugget	1.96E-7	0.304	0.250	0.702	0.3649	0.430
	model type	C_{exp}	C_{Gauss}	C_{Gauss}	C_{Gauss}	C_{Gauss}	C_{Gauss}
	sill	1.311	0.398	0.400	1.150	1.666	1.690
	range (m)	4.826	3.308	3.00	3.260	3.784	5.628
V/U_*	nugget	0.010	0.040	0.040	0.039	4.13E-10	0.025
	model type	C_{Gauss}	C_{exp}	—	—	C_{exp}	C_{exp}
	sill	0.040	4.03E5	—	—	0.050	0.010
	range (m)	4.500	3.97E8	—	—	1.440	2.00
W/U_*	nugget	0.186	0.107	0.050	0.081	0.156	0.050
	model type	C_{Gauss}	C_{Gauss}	C_{exp}	C_{exp}	C_{Gauss}	C_{exp}
	sill	1580	0.970	0.400	0.297	0.376	0.400
	range (m)	451.8	7.207	6.00	8.48	4.964	8.00
u'/U_*	nugget	0.025	0.005	0.027	0.033	0.005	0.010
	model type	—	C_{Gauss}	—	C_{Gauss}	C_{exp}	C_{exp}
	sill	—	0.015	—	0.038	0.025	0.025
	range (m)	—	3.00	—	12.18	3.00	2.00
v'/U_*	nugget	0.042	0.05	0.030	0.025	0.020	8.00E-9
	model type	—	—	—	C_{Gauss}	C_{exp}	C_{exp}
	sill	—	—	—	0.035	0.070	0.036
	range (m)	—	—	—	3.00	2.50	1.416
w'/U_*	nugget	0.005	0.007	0.005	0.005	0.0003	0.006
	model type	C_{Gauss}	C_{exp}	C_{Gauss}	C_{Gauss}	C_{exp}	C_{exp}
	sill	0.005	8.45E4	0.005	0.018	0.018	0.015
	range (m)	3.00	3.63E8	5.00	3.00	4.104	30.80

Figure captions

Figure 1: a) Location of the study reach on the North Fork Cache La Poudre River; b) photograph of the riffle, looking upstream at a discharge of 3.4 m^3/s

Figure 2: Residual semivariogram of bed elevation used to define the covariance for kriging with a trend. The nugget, range (a), and sill (b) parameters described in the text are indicated.

Figure 3: Proportional symbol maps and probability density histograms of non-dimensional streamwise velocity U/U_* at each discharge.

Figure 4: Proportional symbol maps and probability density histograms of non-dimensional vertical velocity V/U_* at each discharge.

Figure 5: Proportional symbol maps and probability density histograms of non-dimensional transverse velocity W/U_* at each discharge.

Figure 6: Proportional symbol maps and probability density histograms of non-dimensional streamwise turbulence intensity u'/U_* at each discharge.

Figure 7: Proportional symbol maps and probability density histograms of non-dimensional vertical turbulence intensity v'/U_* at each discharge.

Figure 8: Proportional symbol maps and probability density histograms of non-dimensional transverse turbulence intensity w'/U_* at each discharge.

Figure 9: Streamwise (top row) and transverse (bottom row) directional semivariograms for each component of the non-dimensional mean velocity at each discharge. Covariance model parameters are given in Table 7.

Figure 10: Streamwise (top row) and transverse (bottom row) directional semivariograms for each component of non-dimensional turbulence intensity at each discharge. Covariance model parameters are given in Table 7.

Figure 11: Streamwise (top row) and transverse (bottom row) directional cross-correlograms between each component of the non-dimensional mean velocity and the local relative roughness h/k_s at each discharge. Error bars indicate one standard error.

Figure 12: Streamwise (top row) and transverse (bottom row) directional cross-correlograms between each component of non-dimensional turbulence intensity and the local relative roughness h/k_s at each discharge. Error bars indicate one standard error.

Figure 13: Thalweg vertical profiles for each component of the non-dimensional mean velocity at each discharge (top three rows). Longitudinal profiles of local roughness height k_s and bed elevation are plotted in the bottom two panels.

Figure 14: Thalweg vertical profiles for each component of non-dimensional turbulence intensity at each discharge (top three rows). Longitudinal profiles of local roughness height k_s and bed elevation are plotted in the bottom two panels.

Figure 1.

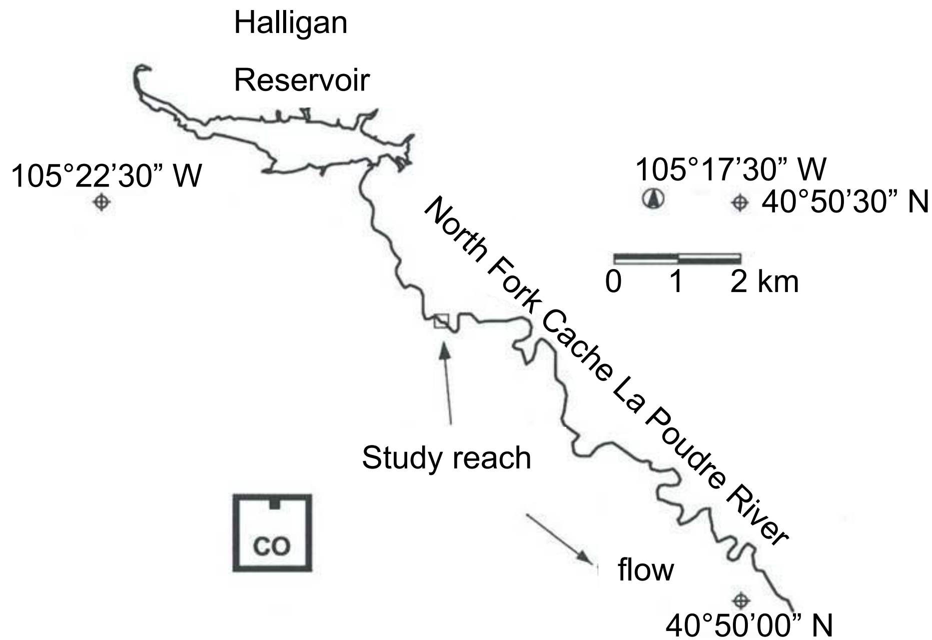
Halligan
Reservoir
105°22'30" W
105°17'30" W
40°50'30" N
0 1 2 km
North Fork Cache La Poudre River
Study reach
CO
flow
40°50'00" N

a)

b)

Figure 2.

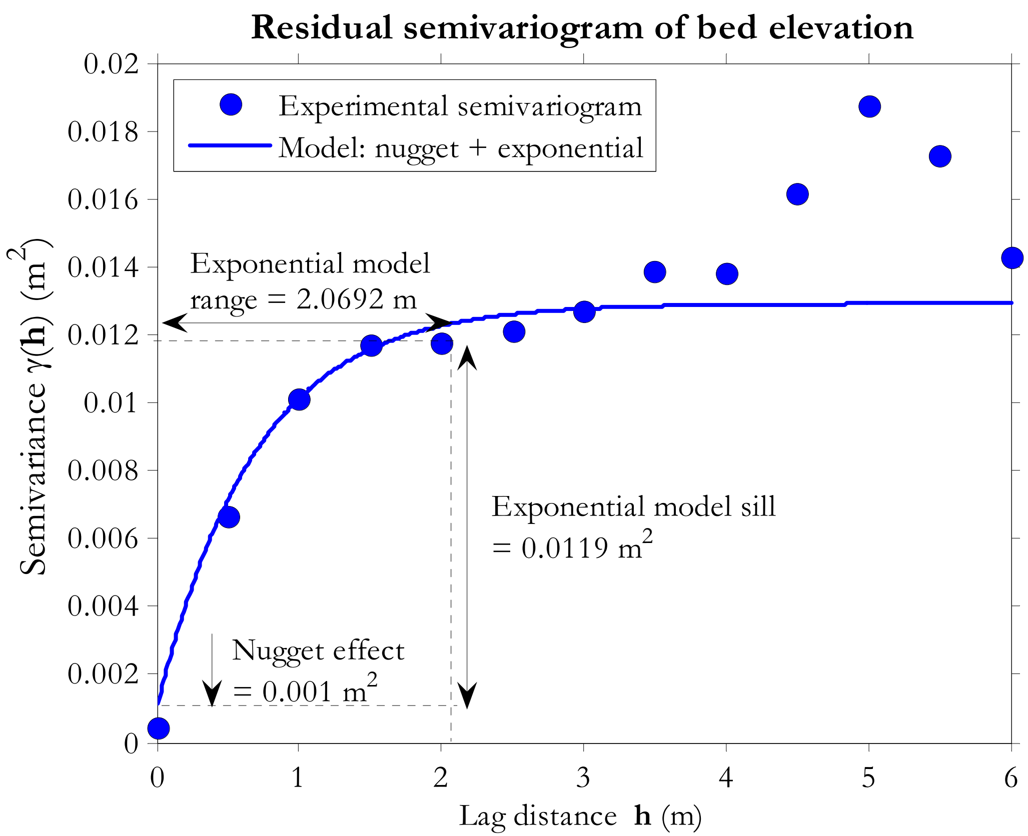

Residual semivariogram of bed elevation
Experimental semivariogram
Model: nugget + exponential
Exponential model
range = 2.0692 m
Exponential model sill
= 0.0119 m2
Nugget effect
= 0.001 m2
Semivariance γ(h) (m2)
Lag distance h (m)
0.02
0.018
0.016
0.014
0.012
0.01
0.008
0.006
0.004
0.002
0
0
1
2
3
4
5
6

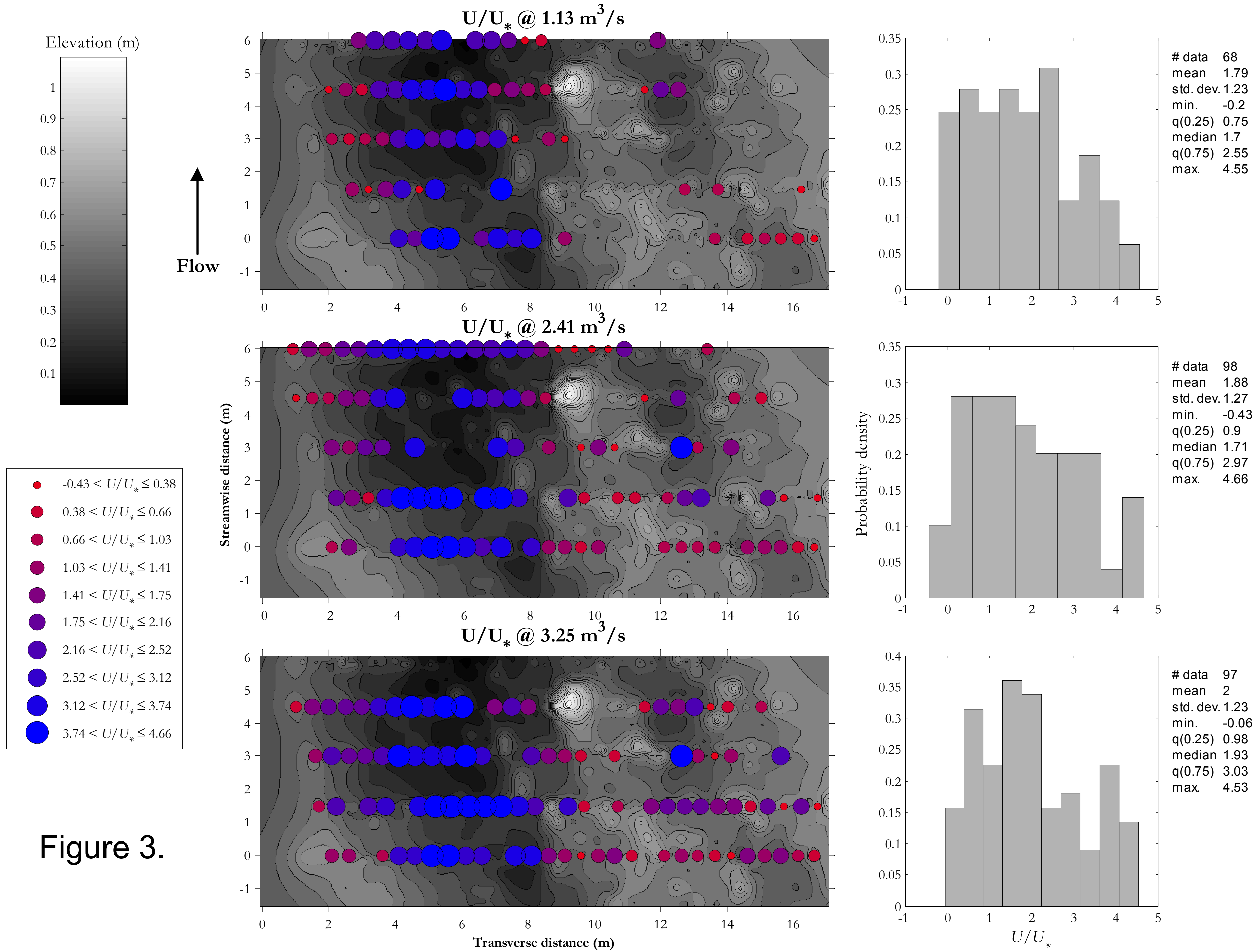

U/U* @ 1.13 m3/s
U/U* @ 2.41 m3/s
U/U* @ 3.25 m3/s
Elevation (m)
Flow
Streamwise distance (m)
Transverse distance (m)
Probability density
U/U*
-0.43 < U/U* ≤ 0.38
0.38 < U/U* ≤ 0.66
0.66 < U/U* ≤ 1.03
1.03 < U/U* ≤ 1.41
1.41 < U/U* ≤ 1.75
1.75 < U/U* ≤ 2.16
2.16 < U/U* ≤ 2.52
2.52 < U/U* ≤ 3.12
3.12 < U/U* ≤ 3.74
3.74 < U/U* ≤ 4.66
data 68
mean 1.79
std. dev. 1.23
min. -0.2
q(0.25) 0.75
median 1.7
q(0.75) 2.55
max. 4.55
data 98
mean 1.88
std. dev. 1.27
min. -0.43
q(0.25) 0.9
median 1.71
q(0.75) 2.97
max. 4.66
data 97
mean 2
std. dev. 1.23
min. -0.06
q(0.25) 0.98
median 1.93
q(0.75) 3.03
max. 4.53

Figure 3.

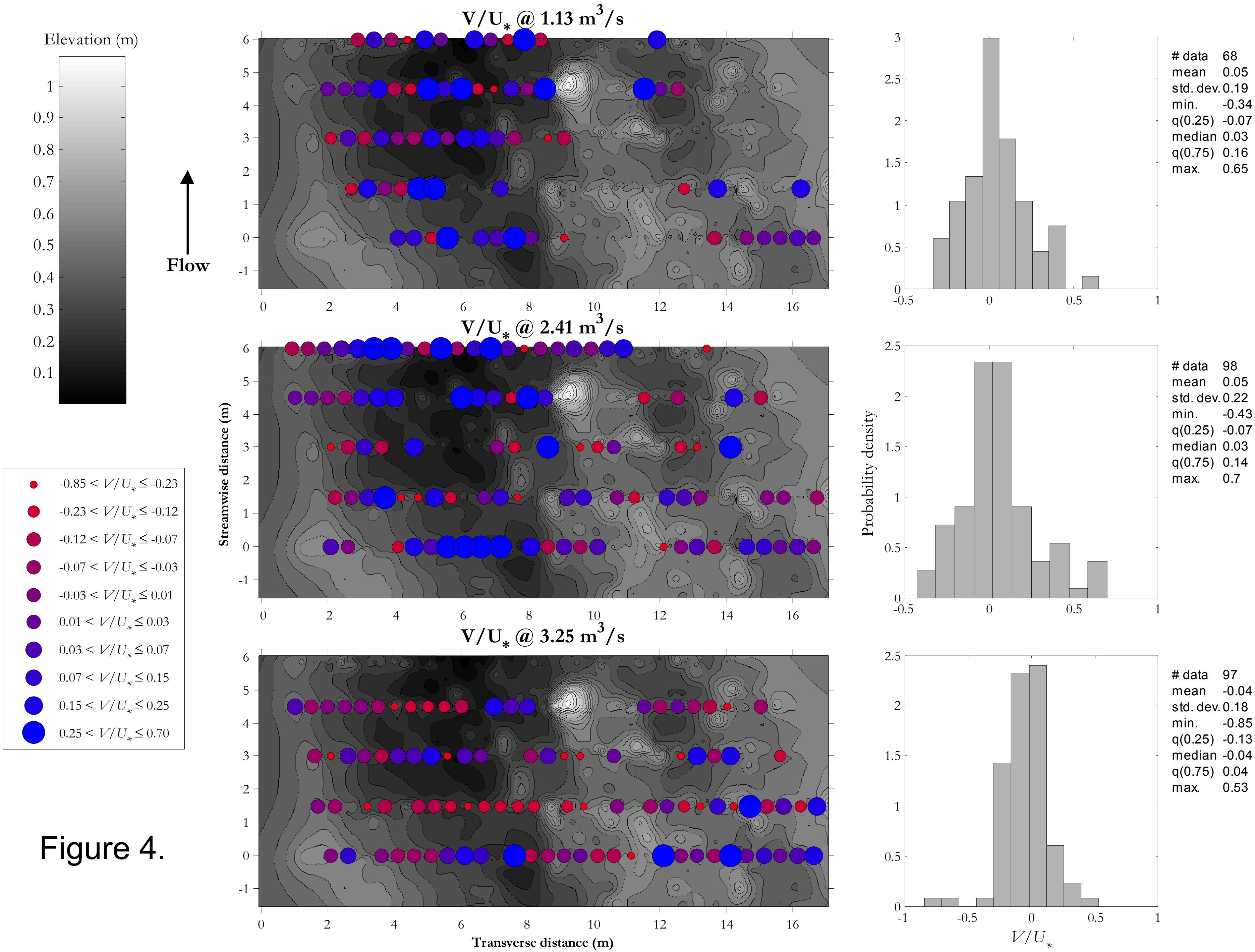

Elevation (m)
Flow
V/U* @ 1.13 m3/s
V/U* @ 2.41 m3/s
V/U* @ 3.25 m3/s
Streamwise distance (m)
Transverse distance (m)
Probability density
V/U*
-0.85 < V/U* ≤ -0.23
-0.23 < V/U* ≤ -0.12
-0.12 < V/U* ≤ -0.07
-0.07 < V/U* ≤ -0.03
-0.03 < V/U* ≤ 0.01
0.01 < V/U* ≤ 0.03
0.03 < V/U* ≤ 0.07
0.07 < V/U* ≤ 0.15
0.15 < V/U* ≤ 0.25
0.25 < V/U* ≤ 0.70
data 68
mean 0.05
std. dev. 0.19
min. -0.34
q(0.25) -0.07
median 0.03
q(0.75) 0.16
max. 0.65
data 98
mean 0.05
std. dev. 0.22
min. -0.43
q(0.25) -0.07
median 0.03
q(0.75) 0.14
max. 0.7
data 97
mean -0.04
std. dev. 0.18
min. -0.85
q(0.25) -0.13
median -0.04
q(0.75) 0.04
max. 0.53

Figure 4.

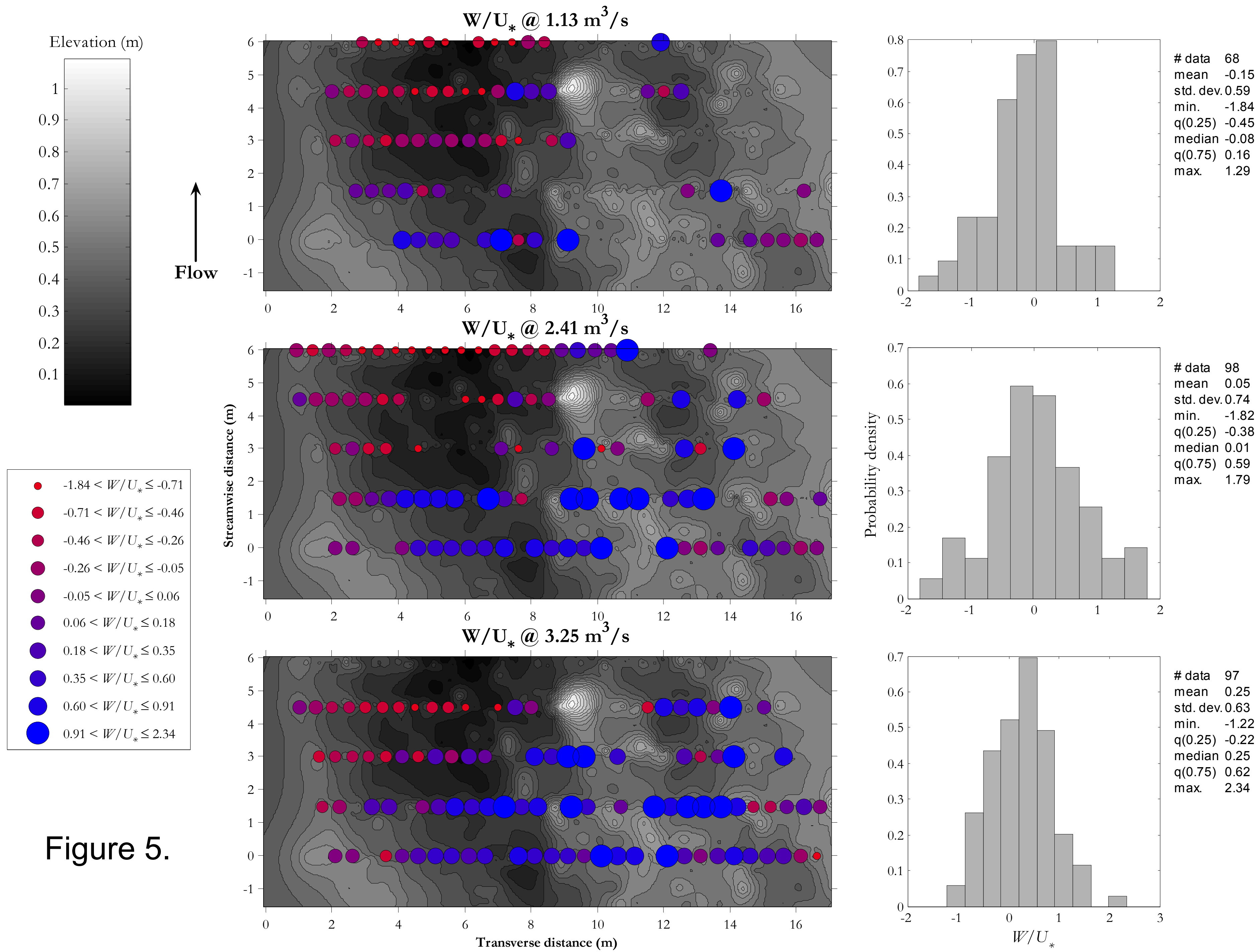

W/U* @ 1.13 m³/s
W/U* @ 2.41 m³/s
W/U* @ 3.25 m³/s
Elevation (m)
Flow
Streamwise distance (m)
Transverse distance (m)
Probability density
W/U*
-1.84 < W/U* ≤ -0.71
-0.71 < W/U* ≤ -0.46
-0.46 < W/U* ≤ -0.26
-0.26 < W/U* ≤ -0.05
-0.05 < W/U* ≤ 0.06
0.06 < W/U* ≤ 0.18
0.18 < W/U* ≤ 0.35
0.35 < W/U* ≤ 0.60
0.60 < W/U* ≤ 0.91
0.91 < W/U* ≤ 2.34
data 68
mean -0.15
std. dev. 0.59
min. -1.84
q(0.25) -0.45
median -0.08
q(0.75) 0.16
max. 1.29
data 98
mean 0.05
std. dev. 0.74
min. -1.82
q(0.25) -0.38
median 0.01
q(0.75) 0.59
max. 1.79
data 97
mean 0.25
std. dev. 0.63
min. -1.22
q(0.25) -0.22
median 0.25
q(0.75) 0.62
max. 2.34

Figure 5.

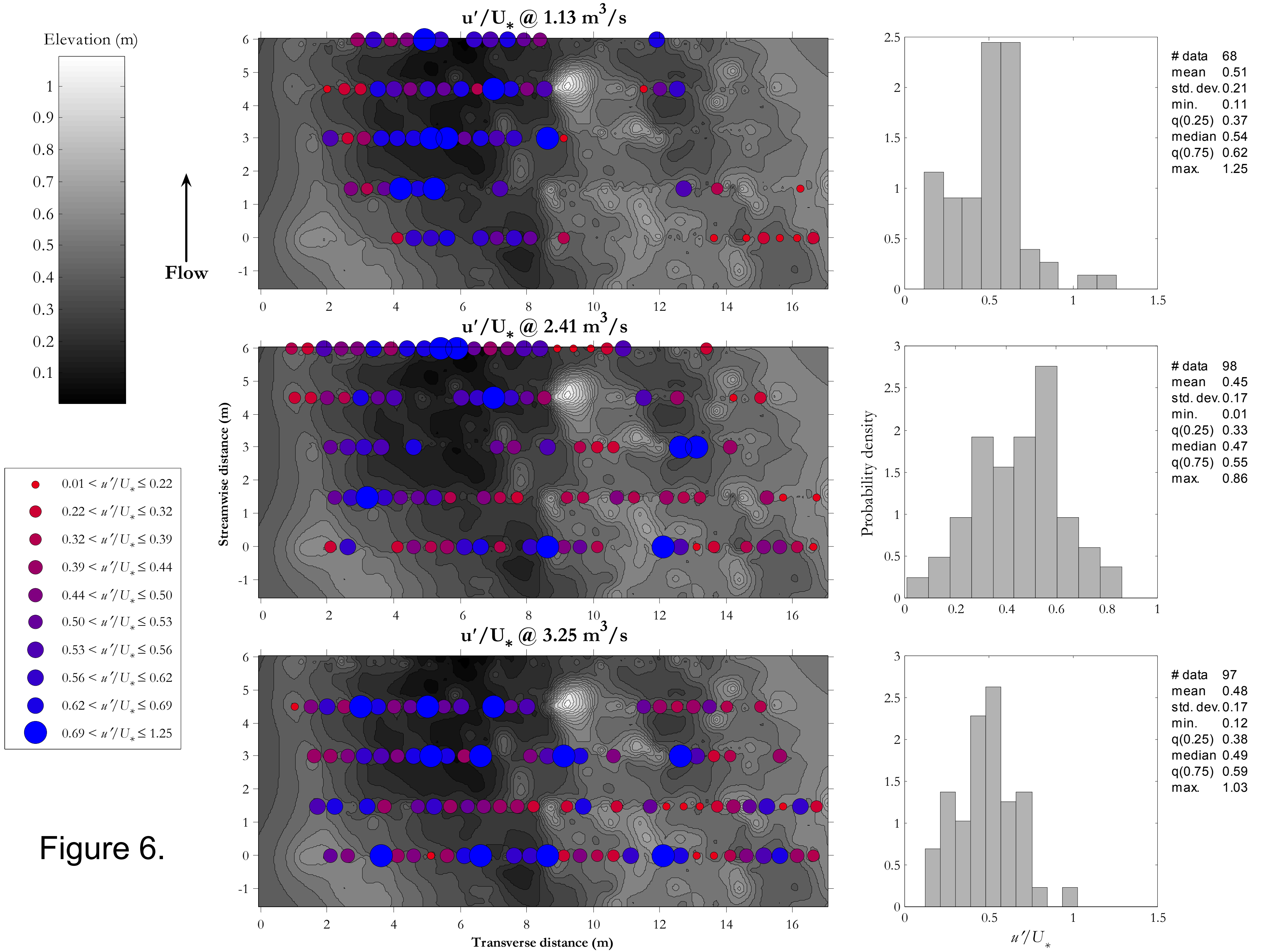
Elevation (m)
Flow
u′/U* @ 1.13 m³/s
u′/U* @ 2.41 m³/s
u′/U* @ 3.25 m³/s
Streamwise distance (m)
Transverse distance (m)
Probability density
u′/U*
0.01 < u′/U* ≤ 0.22
0.22 < u′/U* ≤ 0.32
0.32 < u′/U* ≤ 0.39
0.39 < u′/U* ≤ 0.44
0.44 < u′/U* ≤ 0.50
0.50 < u′/U* ≤ 0.53
0.53 < u′/U* ≤ 0.56
0.56 < u′/U* ≤ 0.62
0.62 < u′/U* ≤ 0.69
0.69 < u′/U* ≤ 1.25
data 68
mean 0.51
std. dev. 0.21
min. 0.11
q(0.25) 0.37
median 0.54
q(0.75) 0.62
max. 1.25
data 98
mean 0.45
std. dev. 0.17
min. 0.01
q(0.25) 0.33
median 0.47
q(0.75) 0.55
max. 0.86
data 97
mean 0.48
std. dev. 0.17
min. 0.12
q(0.25) 0.38
median 0.49
q(0.75) 0.59
max. 1.03

Figure 6.

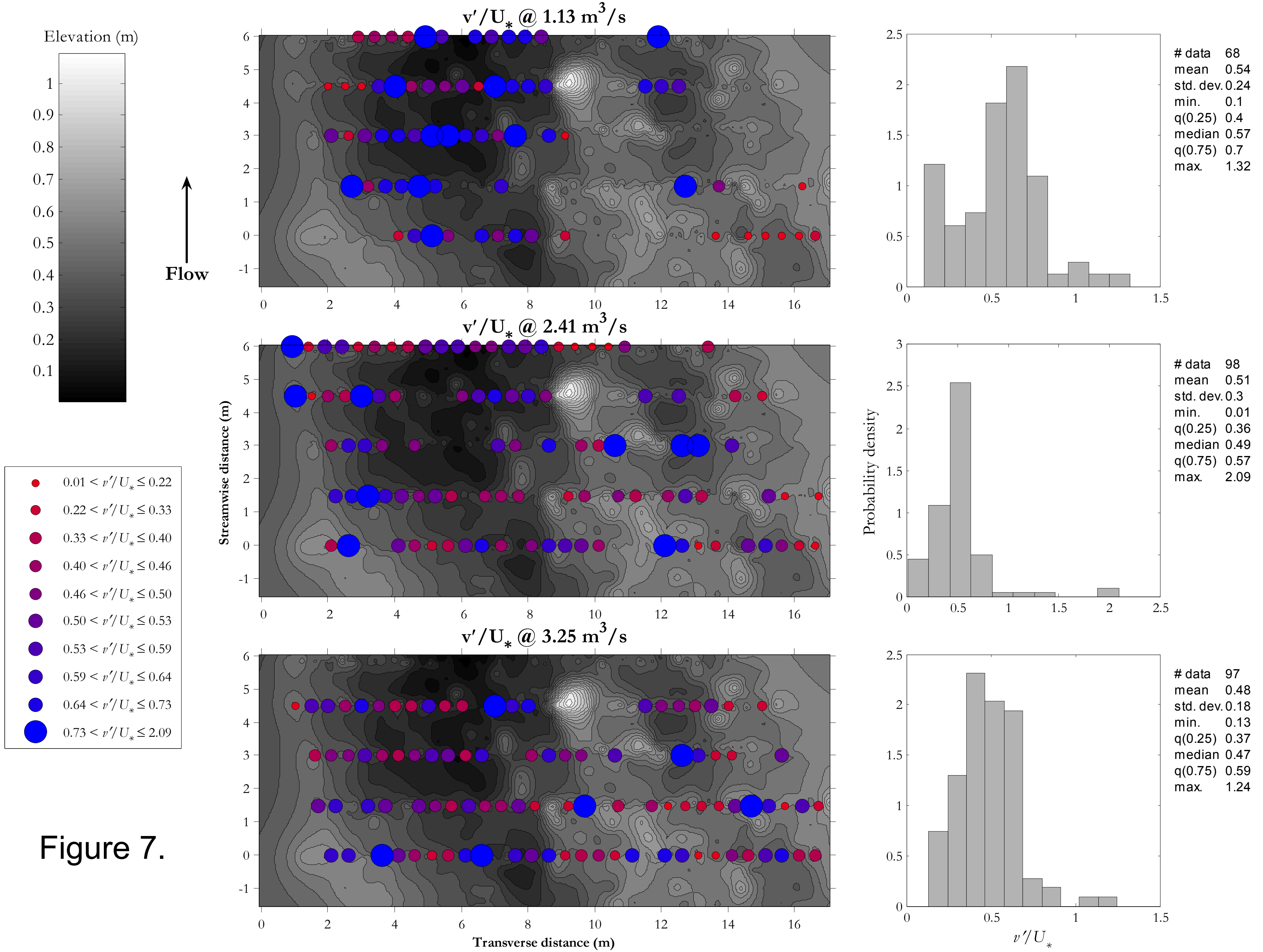

Elevation (m)
Flow
v′/U* @ 1.13 m3/s
v′/U* @ 2.41 m3/s
v′/U* @ 3.25 m3/s
Streamwise distance (m)
Transverse distance (m)
Probability density
v′/U*
0.01 < v′/U* ≤ 0.22
0.22 < v′/U* ≤ 0.33
0.33 < v′/U* ≤ 0.40
0.40 < v′/U* ≤ 0.46
0.46 < v′/U* ≤ 0.50
0.50 < v′/U* ≤ 0.53
0.53 < v′/U* ≤ 0.59
0.59 < v′/U* ≤ 0.64
0.64 < v′/U* ≤ 0.73
0.73 < v′/U* ≤ 2.09
data 68
mean 0.54
std. dev. 0.24
min. 0.1
q(0.25) 0.4
median 0.57
q(0.75) 0.7
max. 1.32
data 98
mean 0.51
std. dev. 0.3
min. 0.01
q(0.25) 0.36
median 0.49
q(0.75) 0.57
max. 2.09
data 97
mean 0.48
std. dev. 0.18
min. 0.13
q(0.25) 0.37
median 0.47
q(0.75) 0.59
max. 1.24

Figure 7.

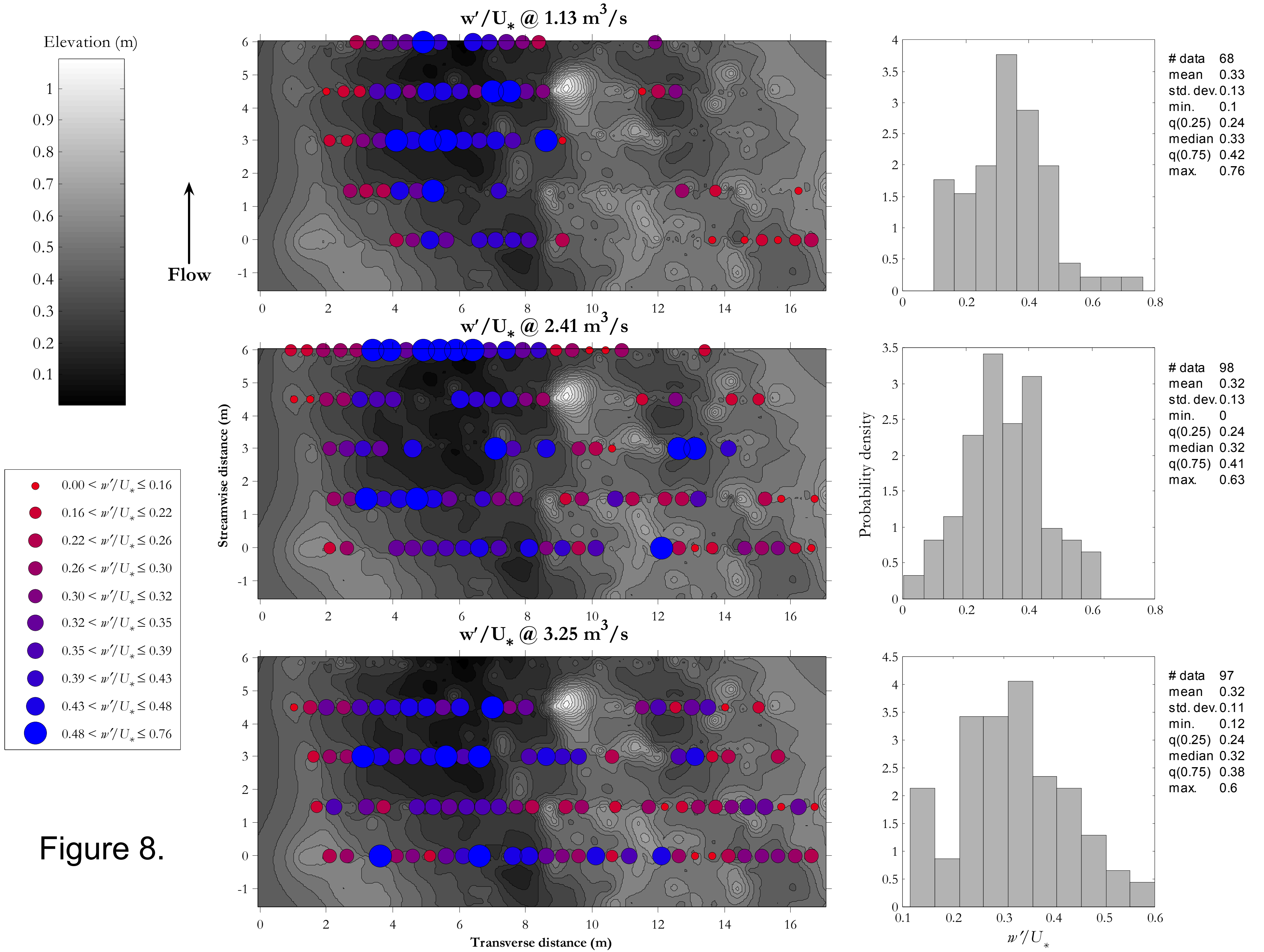
Elevation (m)
Flow
w′/U* @ 1.13 m³/s
w′/U* @ 2.41 m³/s
w′/U* @ 3.25 m³/s
Streamwise distance (m)
Transverse distance (m)
Probability density
w′/U*
0.00 < w′/U* ≤ 0.16
0.16 < w′/U* ≤ 0.22
0.22 < w′/U* ≤ 0.26
0.26 < w′/U* ≤ 0.30
0.30 < w′/U* ≤ 0.32
0.32 < w′/U* ≤ 0.35
0.35 < w′/U* ≤ 0.39
0.39 < w′/U* ≤ 0.43
0.43 < w′/U* ≤ 0.48
0.48 < w′/U* ≤ 0.76
data 68
mean 0.33
std. dev. 0.13
min. 0.1
q(0.25) 0.24
median 0.33
q(0.75) 0.42
max. 0.76
data 98
mean 0.32
std. dev. 0.13
min. 0
q(0.25) 0.24
median 0.32
q(0.75) 0.41
max. 0.63
data 97
mean 0.32
std. dev. 0.11
min. 0.12
q(0.25) 0.24
median 0.32
q(0.75) 0.38
max. 0.6

Figure 8.

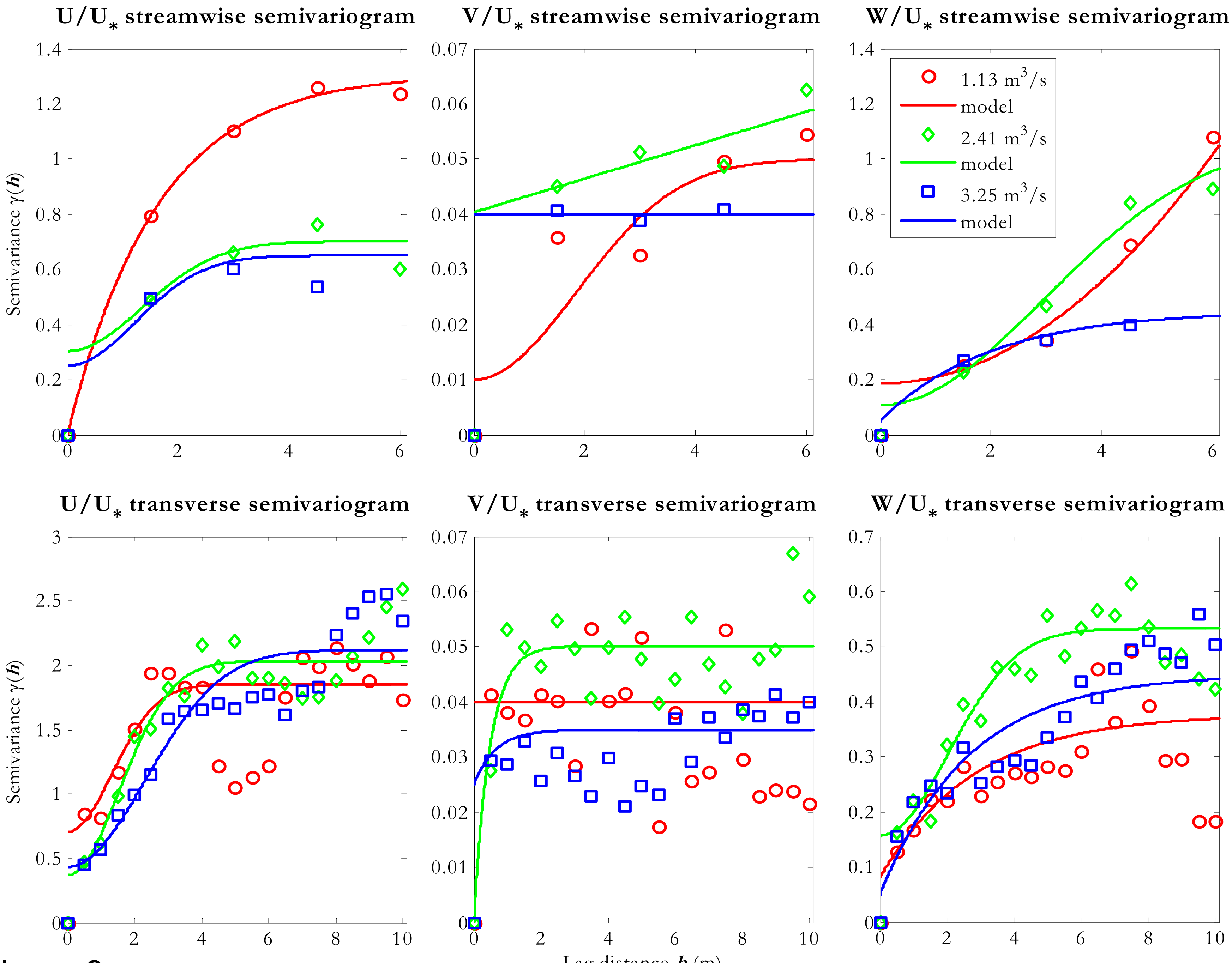
U/U* streamwise semivariogram
V/U* streamwise semivariogram
W/U* streamwise semivariogram
U/U* transverse semivariogram
V/U* transverse semivariogram
W/U* transverse semivariogram
Semivariance γ(h)
Lag distance h (m)
1.13 m3/s
model
2.41 m3/s
model
3.25 m3/s
model

Figure 9.

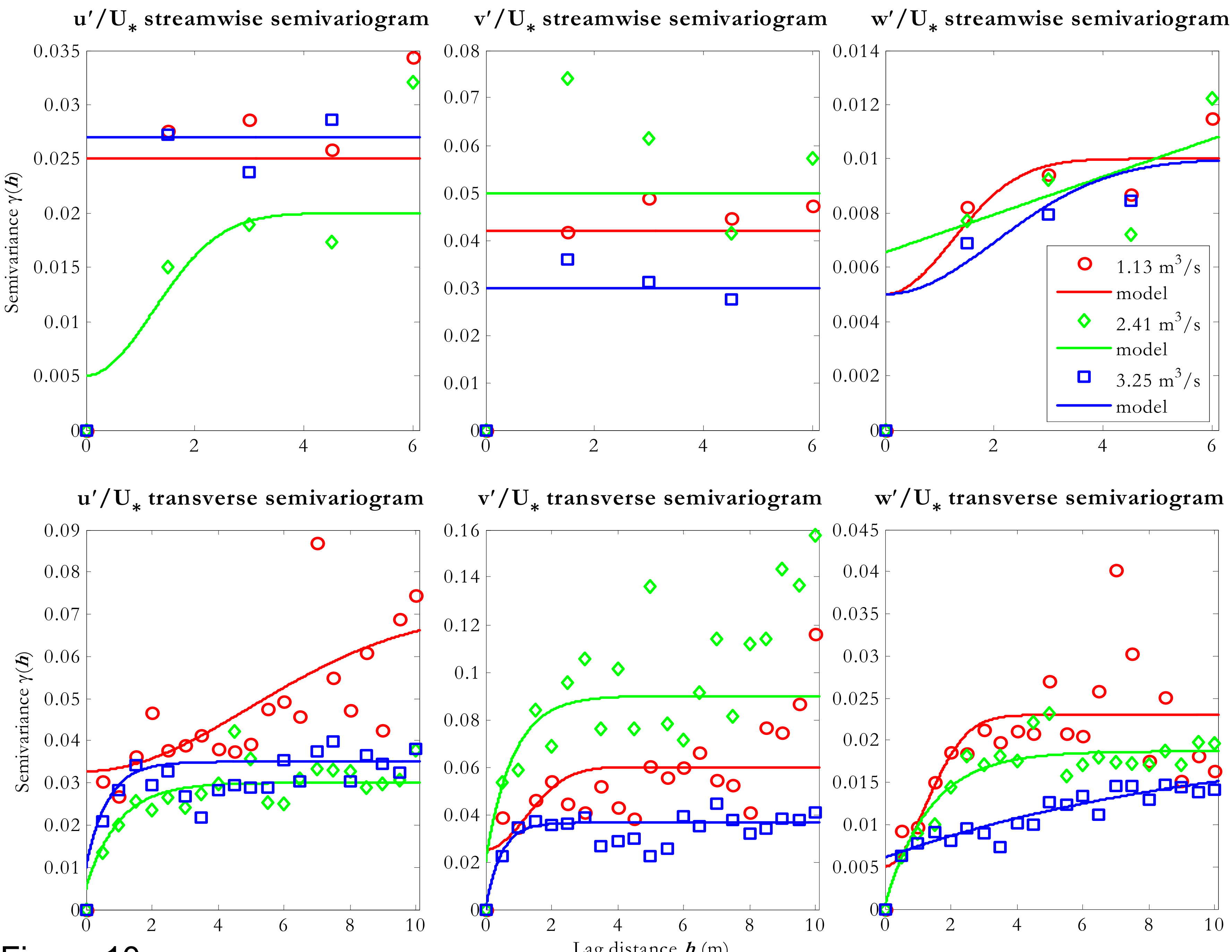
u′/U* streamwise semivariogram
v′/U* streamwise semivariogram
w′/U* streamwise semivariogram
u′/U* transverse semivariogram
v′/U* transverse semivariogram
w′/U* transverse semivariogram
Semivariance γ(h)
Lag distance h (m)
1.13 m3/s
model
2.41 m3/s
model
3.25 m3/s
model

Figure 10.

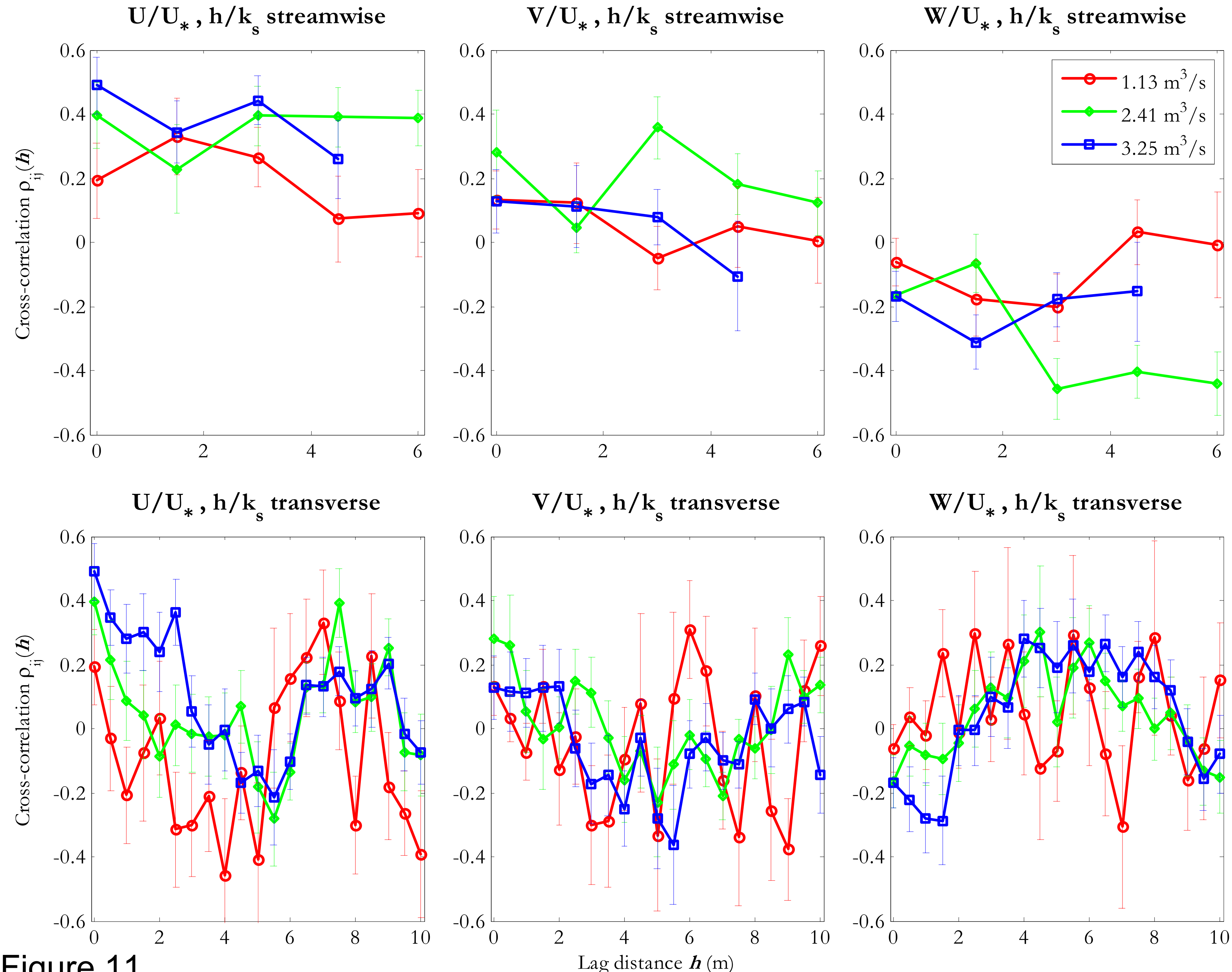
U/U*, h/ks streamwise
V/U*, h/ks streamwise
W/U*, h/ks streamwise
1.13 m3/s
2.41 m3/s
3.25 m3/s
U/U*, h/ks transverse
V/U*, h/ks transverse
W/U*, h/ks transverse
Cross-correlation ρij(h)
Lag distance h (m)

Figure 11.

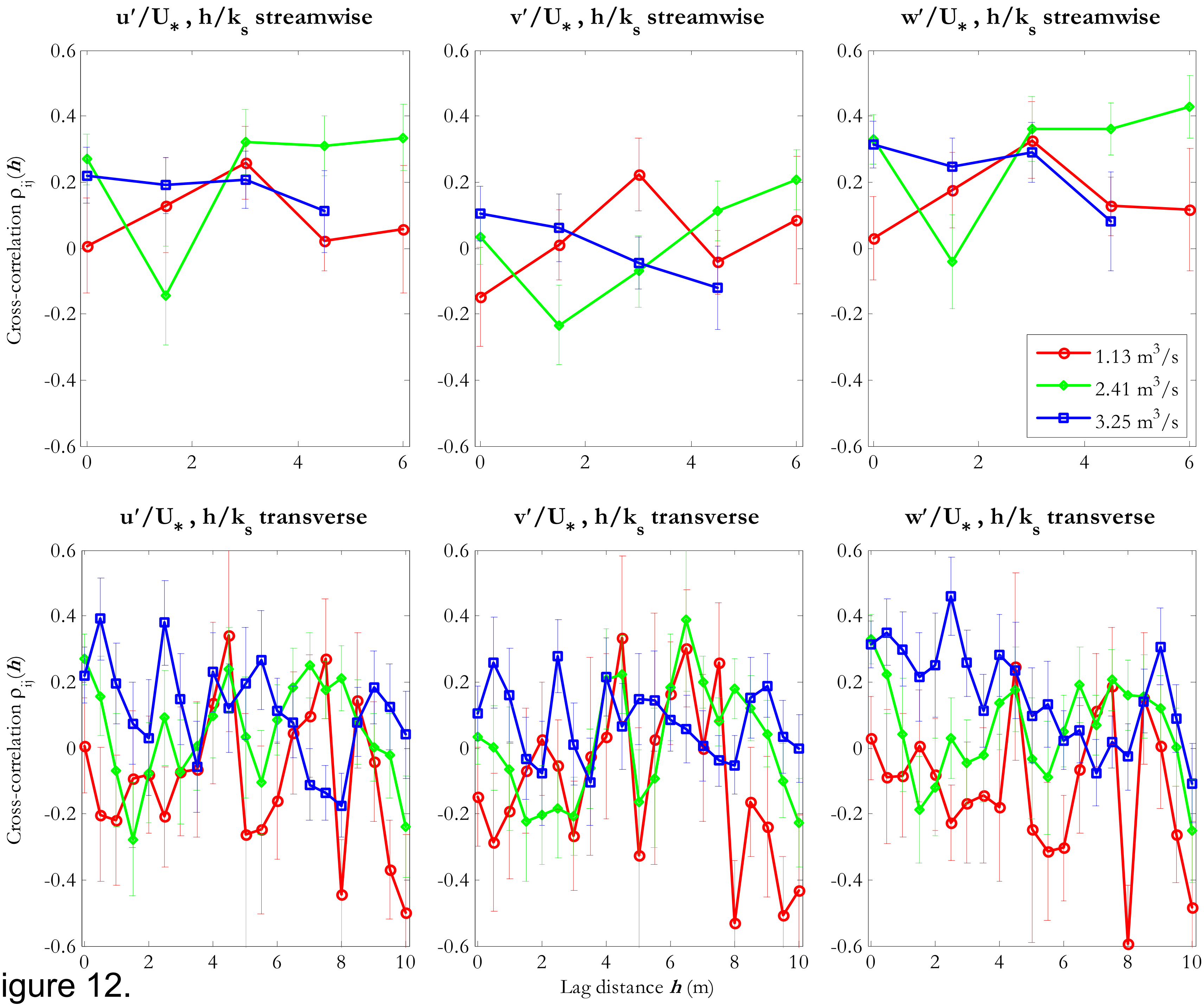

u′/U∗ , h/ks streamwise
v′/U∗ , h/ks streamwise
w′/U∗ , h/ks streamwise
u′/U∗ , h/ks transverse
v′/U∗ , h/ks transverse
w′/U∗ , h/ks transverse
Cross-correlation ρij(h)
Lag distance h (m)
1.13 m3/s
2.41 m3/s
3.25 m3/s

Figure 12.

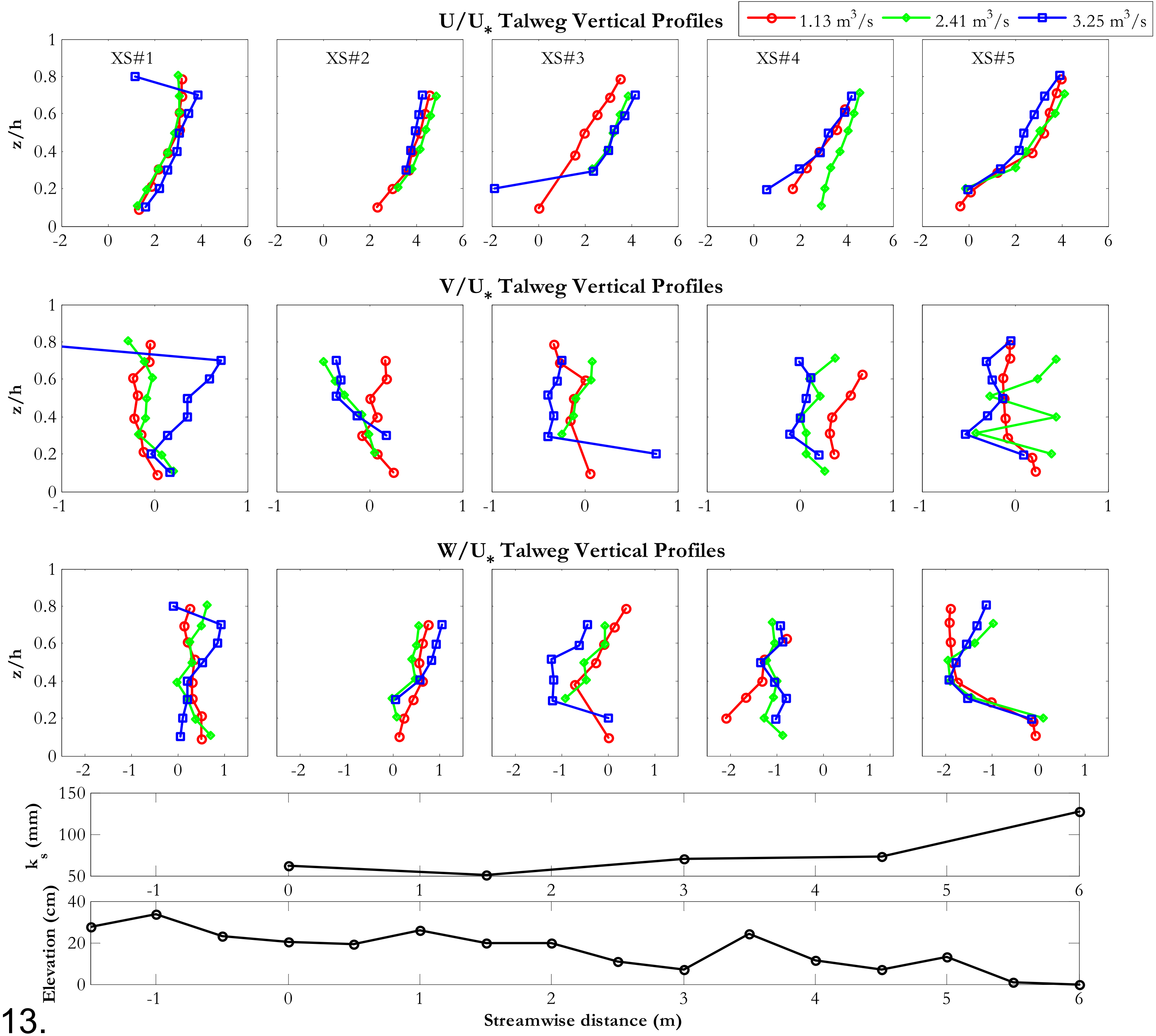
U/U* Talweg Vertical Profiles
1.13 m^3/s
2.41 m^3/s
3.25 m^3/s
XS#1
XS#2
XS#3
XS#4
XS#5
z/h
V/U* Talweg Vertical Profiles
W/U* Talweg Vertical Profiles
k_s (mm)
Elevation (cm)
Streamwise distance (m)

Figure 13.

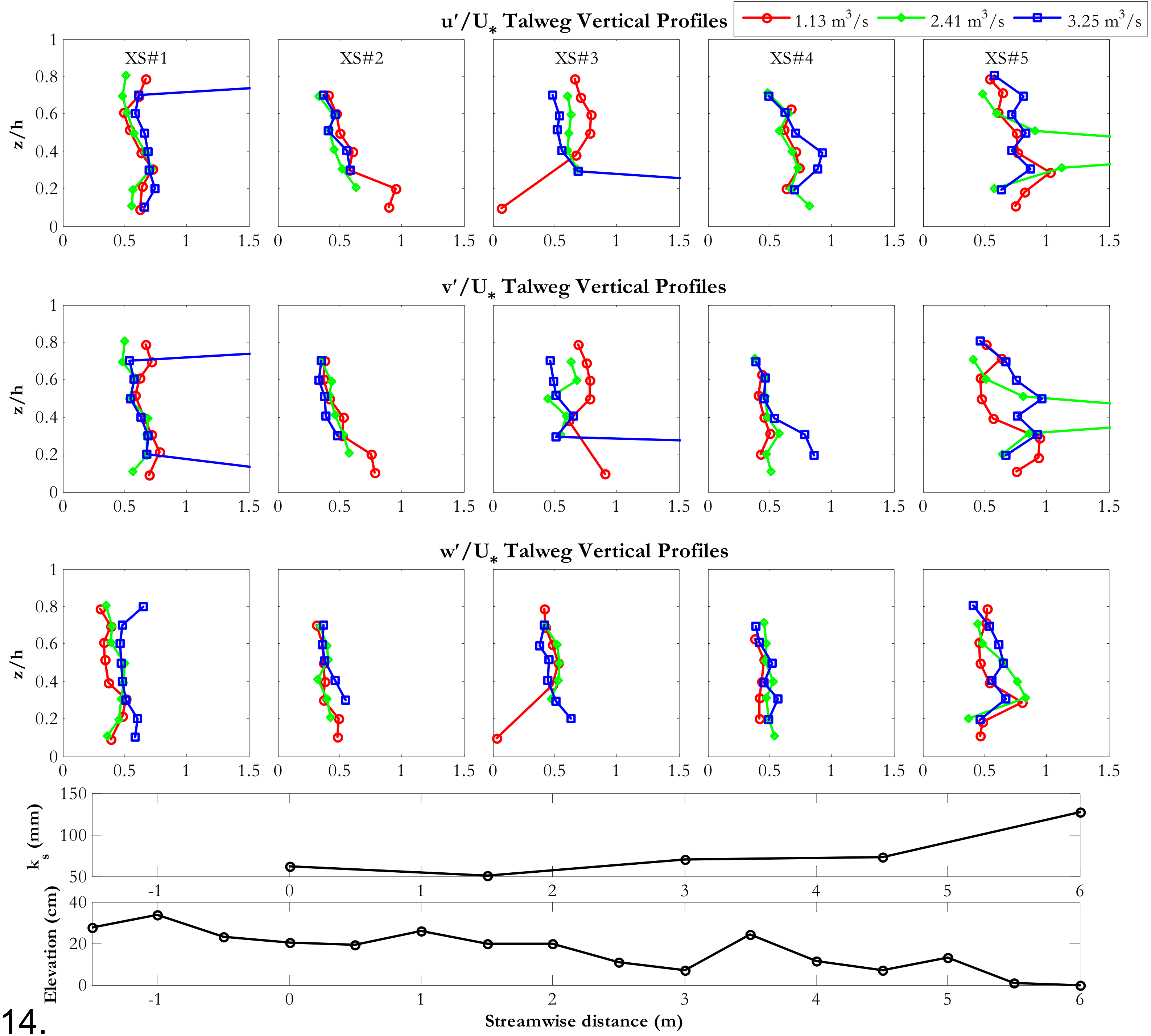

u′/U* Talweg Vertical Profiles
1.13 m3/s
2.41 m3/s
3.25 m3/s
XS#1
XS#2
XS#3
XS#4
XS#5
z/h
v′/U* Talweg Vertical Profiles
w′/U* Talweg Vertical Profiles
ks (mm)
Elevation (cm)
Streamwise distance (m)

Figure 14.